UC Santa Cruz
UC Santa Cruz Electronic Theses and Dissertations

Title

Computing Slowly Moving Shocks with Flux-differencing Schemes

Permalink

https://escholarship.org/uc/item/7255g3js

Author

Lavell, Michael

Publication Date

2017

Peer reviewed|Thesis/dissertation

UNIVERSITY OF CALIFORNIA

SANTA CRUZ

Computing Slowly Moving Shocks with Flux-differencing Schemes

A thesis submitted in partial satisfaction

of the requirements for the degree of

MASTER OF SCIENCE

in

SCIENTIFIC COMPUTING AND APPLIED MATHEMATICS

by

Michael Lavell

June 2017

The thesis of Michael Lavell is approved by:

_____

Professor Dongwook Lee, Chair

_____

Professor Nicholas Brummell

_____

Professor Pascale Garaud

_____

Dean Tyrus Miller

Vice Provost and Dean of Graduate Studies

Contents

List of Figures

Abstract

Computing slowly moving shocks with flux-differencing schemes

by

Michael Lavell

The numerical error produced when computing slowly moving shocks in a finite volume framework is studied. The error is a result of discretizing a thin shock profile dynamic on the scale of spatial and temporal discretization. It has been studied in great detail by many practitioners, but no fix has been built to totally eradicate the problem unique to nonlinear hyperbolic systems. I argue that current shock capturing schemes do not accurately resolve the nonlinear shock profile and this results in erroneous oscillations. I study numerical tools used to pursue high-order accurate solutions of slow shocks, including a hybridized upwind-biased slope limiter for the piecewise parabolic method, a universal Osher Riemann solver, and a new weighted essentially non-oscillatory (WENO)-type slope limiter. The effectiveness of these tools are tested in two hyperbolic systems: the Euler equations and the ideal magnetohydrodynamics equations. The success of the upwind-biased slope limiter has been verified against high-order accurate schemes such as WENO.

Acknowledgements

Thank you Dongwook, Nic, and Pascale for all of your support!

1. Introduction

Advances in high-performance computing and computational mathematics allow us to model physics with extreme precision. Subjects difficult and expensive to study, such as astrophysical plasmas, confinement experiments, and vehicle aerodynamics, are easily accessible thanks to computational fluid dynamics. Finite volume methods (FVM), also known as Godunov-type schemes or flux-differencing schemes, evolve volume-averaged conserved quantities across a discretized domain to approximate flows. This is done by building approximating n^th degree piecewise polynomials on each cell of the discretized domain, extrapolating cell boundary values, and solving the Riemann problem at each cell interface. These methods are very popular because of their ability to accurately capture flows with sharp shocks and discontinuities.

Conservative systems, such as the Euler's equations and ideal magnetohydrodynamics (MHD) equations, consider the evolution of conserved quantities with varying complexity. The ability to capture gas dynamics governed by the ideal MHD equations are of particular interest because of the inherently more complex structures and environments they model. Eq.(1) is a conservative formulation of the ideal MHD equations with the additional constraint $\nabla \cdot \vec{B} = 0$.

$$
\begin{cases}
\frac{\partial \rho}{\partial t} + \nabla \cdot (\rho \vec{v}) = 0 \\
\frac{\partial \rho \vec{v}}{\partial t} + \nabla \cdot \left(\rho \vec{v}\vec{v} + \vec{I}(P + \frac{1}{2}B^2) - \vec{B}\vec{B} \right) = 0 \\
\frac{\partial E}{\partial t} + \nabla \cdot \left((E + P + \frac{1}{2\mu_0}B^2)\vec{v} - \vec{B}(\vec{v} \cdot \vec{B}) \right) = 0 \\
\frac{\partial \vec{B}}{\partial t} + \nabla \cdot (\vec{v}\vec{B} - \vec{B}\vec{v}) = 0
\end{cases}
\tag{1}
$$

The quantities that define the ideal MHD equations are density ρ, velocity $\vec{v}$, energy E, pressure P and magnetic field $\vec{B}$. The constant μ_0 is the magnetic permeability in a vacuum. The equation of state is given by

$$
\frac{d}{dt}\left(\frac{p}{\rho^\gamma} \right) = 0,
\tag{2}
$$

where γ is the ratio of specific heats.

Shocks are small regions of sharp gradients in which a gas property changes from one equilibrium state to another. Numerically capturing the evolution and interaction of these properties requires discretizing space and defining an originally continuous profile at a finite number of points. Solutions to smooth flows and flows with fast moving shocks generally behave well for most modern numerical methods. A problem arises when a shock is dynamic on the scale of the grid discretization and time step. This phenomenon is referred to as the "slowly moving shock" problem. Numerically modeling a slowly moving shock, or a shock that requires multiple time steps Δt to cross a cell of size Δx, produces post-shock oscillations that pollute the numerical solution. Figure 1 illustrates slowly moving shocks in the ideal MHD equations and the full Euler equations.

Shown in Figures 1a and 1b are numerical experiments of the Brio-Wu MHD shock tube and in Figures 1c and 1d are numerical experiments of the hydrodynamics (HD) slow shock experiment. These tests will be constructed and discussed in greater detail in Section 5. At $t = 0.1$, both experiments have a left-running shock front that has been displaced by approximately $\Delta x = 0.3$. Thus, the shock speed is $S \approx 0.03$. The oscillations in the density profiles are evident in (b) and (d). Notice in (d) that the oscillations persist in the WENO-Z solution computed with Runge Kutta 4 (RK4) on a grid size of $N = 2048$. Increasing the order of spatial reconstruction or grid resolution does not converge to the true solution, however the high-resolution WENO-Z solution is considered a close approximation to the analytic solution.

The non-physical oscillations that develop upwind of slowly moving shocks have been studied in great detail [1, 2, 3, 4, 5, 6, 7, 8, 9]. Most reconstruction schemes produce unphysical oscillations in discontinuous solutions for nonlinear hyperbolic systems, with higher-order accurate methods producing greater amplitude oscillations. Higher-order methods have less numerical dissipation, and consequently, their solutions at slowly moving shocks maintain large amplitude spurious oscillations. Multiple studies note the size of the error is dependent on the nonlinearity of the problem and the speed of shock. Greater nonlinearity

2

(a)

(b)

(c)

(d)
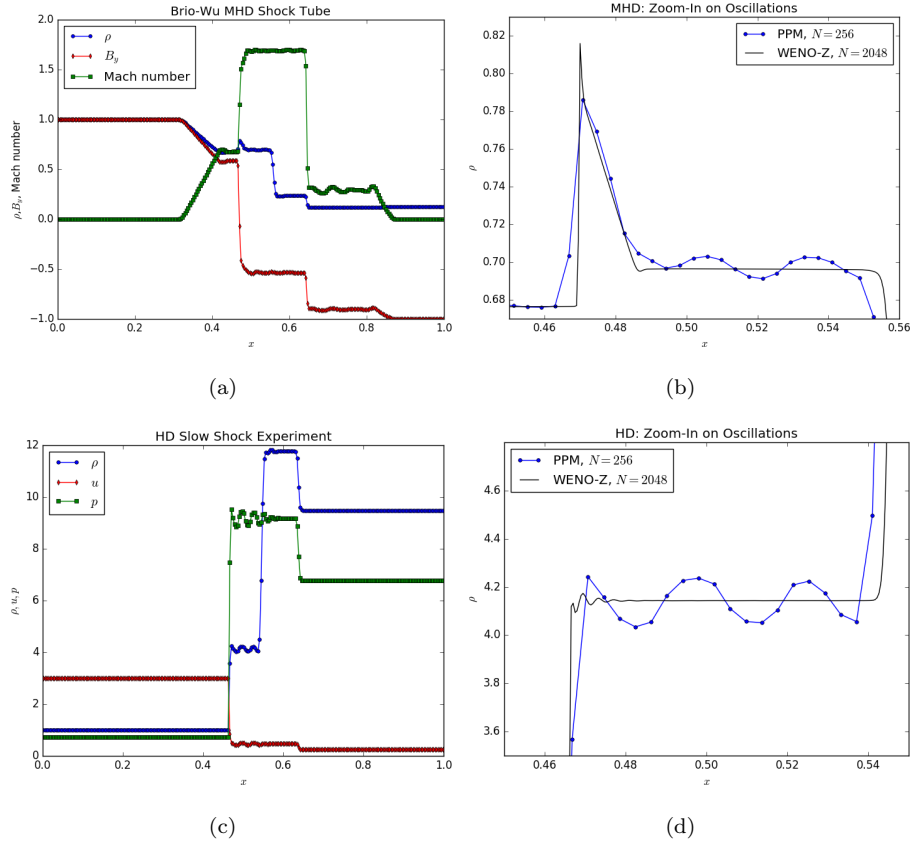
Figure 1: (a) and (b) are the Brio-Wu MHD shock tube at $t = 0.1$ computed with PPM, a grid size of $N = 256$, CFL$= 0.8$, the Roe Riemann solvers, and MC slope limiter. (c) and (d) are the HD slow shock experiment at $t = 0.1$ computed with PPM, a grid size of $N = 256$, CFL $= 0.8$, the Roe Riemann solvers, and MC slope limiter. The high-resolution WENO-Z solution is computed with a grid size of $N = 2048$, CFL $= 0.8$, the Roe Riemann solvers, and MC slope limiter.

3

and slower shock speed result in larger oscillations.

It is important to overcome this problem for flow regimes dependent on small scale structures and for methods computing steady solutions. Fine scale structures are vital to the overall study in modeling environments such as detonation simulations, computational aeroacoustics, and turbulence. Seeking a steady solution can require many time steps for a profile to converge to a true solution. Erroneous oscillations that potentially pollute the solution profile will interfere with a method's ability to produce a stable solution that is to converge to a physically correct weak solution.

2. Numerical methods for flux-differencing schemes

An important set of methods for computational fluid dynamics are the flux-differencing schemes. These methods achieve robust solutions for solving smooth and discontinuous flows governed by hyperbolic conservation laws. All conservative systems can be written in the following form,

$$U_t + \nabla \cdot F(U) = 0, \tag{3}$$

where U is the state variable or vector, and $F(U)$ is the analytical flux function.

Following an ordinary differential equation discretization in time of Eq.(3), the numerical solution at time $t = t^n + \Delta t$ for a 1-dimensional problem can be written

$$u_j^{n+1} = u_j^n - \frac{\Delta t}{\Delta x}[\hat{F}_{j+\frac{1}{2}}^{n+\frac{1}{2}} - \hat{F}_{j-\frac{1}{2}}^{n+\frac{1}{2}}]. \tag{4}$$

Here, $\hat{F}_{j+\frac{1}{2}}^{n+\frac{1}{2}}$ is the numerical flux function at the cell interface $x_{j+\frac{1}{2}}$ evaluated at the half-time step advancement. FVM's are also referred to as flux-differencing schemes because the numerical flux function is a sum of the average of analytical fluxs of interpolated solutions and a diffusive flux term resulting from solving the Riemann problem at the cell interface. The numerical flux function takes the form

$$\hat{F}_{j+\frac{1}{2}}^{n+\frac{1}{2}} = \hat{F}_{\text{avg}} + \hat{F}_{\text{diff}}. \tag{5}$$

$\hat{F}_{\text{avg}}$ is an average of the analytical flux evaluated at the half-time step nodal values, $u_{j\pm\frac{1}{2}}^{n+\frac{1}{2}}$, and generally considers the algebraic average:

$$\hat{F}_{\text{avg}} = \frac{1}{2}(F_R + F_L) = \frac{1}{2}\left(F(u_{j+\frac{1}{2}}^{n+\frac{1}{2}}) + F(u_{j-\frac{1}{2}}^{n+\frac{1}{2}})\right). \tag{6}$$

$\hat{F}_{\text{diff}}$ is computed by solving the Riemann problem at the cell interface and acts as a stabilizing term to the average flux [10]. Computational cost and solution accuracy are highly dependent on the numerical flux function chosen to solve the Riemann problem and the degree of the polynomial chosen to extrapolate the nodal values, $u_{j\pm\frac{1}{2}}^{n}$.

2.1. Model equations

In this section, several model equations are introduced that can be studied with conservation laws: the scalar inviscid Burgers' equation, the full Euler equations, the isothermal Euler equations, and the ideal MHD equations.

2.1.1. The inviscid Burgers' equation

The Burgers' equation, written in conservative form, is a scalar nonlinear partial differential equation,

$$u_t + (\frac{u^2}{2})_x = 0. \tag{7}$$

Unlike systems of equations, no post-shock oscillations are produced when computing slowly moving shocks in a scalar equation. This is because in the scalar case the left and right state of the shock can be connected exactly by a single wave solution.

2.1.2. The Euler equations

The full Euler equations consider the conservation of mass, momentum, and energy in an inviscid and adiabatic gas. They are presented here in conservative form.

$$\begin{cases} \rho_t + (\rho u)_x = 0, \\ (\rho u)_t + (\rho u^2 + p)_x = 0, \\ E_t + (u(E + p))_x = 0. \end{cases} \tag{8}$$

The total energy E is the sum of kinetic and internal energies,

$$E = \rho \left(\frac{u^2}{2} + e \right). \tag{9}$$

An isothermal problem is considered to explore the phase space of the internal shock structure [3]. In the case of a simple gamma-law equation of state, the dynamics in pressure can be eliminated by setting γ to be approximately one, i.e. $\gamma = 1.0001$. The equation of state state reduces to being dependent only on the density and speed of sound a:

$$p = \rho R T = \rho(R\bar{T}) = \rho \left(\frac{p}{\rho} \right) \approx \rho \left(\frac{\gamma p}{\rho} \right) = \rho a^2. \tag{10}$$

The third-order system reduces to the second-order system describing an isothermal gas:

$$\begin{cases} \rho_t + (\rho u)_x = 0 \\ (\rho u)_t + (\rho(u^2 + a^2))_x = 0 \end{cases} \tag{11}$$

Considering the same numerical experiment as the full Euler equations, the discrete shock structure can be studied in the two-dimensional state space $(\rho, \rho u)$ of the isothermal Euler equations. The phase plots of a discrete shock are created by extracting the few points that lie within the shock region at a given time t^n. An experiment must be observed at many different time steps to create a descriptive phase plot.

2.1.3. The ideal MHD equations

The ideal MHD equations describe the behavior of a charged gas in the presence of a magnetic field. The conservative MHD formulation Eq.(1) is equivalent to substituting the following conservative variables and flux function into Eq.(3),

$$
U = \begin{bmatrix} \rho \\ \rho u_x \\ \rho u_y \\ \rho u_z \\ B_y \\ B_z \\ E \end{bmatrix} \qquad F(U) = \begin{bmatrix} \rho u_x \\ \rho u_x^2 + p^* - B_x^2 \\ \rho u_x u_y - B_x B_y \\ \rho u_x u_z - B_x B_z \\ B_y u_x - B_x u_y \\ B_z u_x - B_x u_z \\ (E + p^*) u_x - B_x (B_x u_x + B_y u_y + B_z u_z) \end{bmatrix} . \qquad (12)
$$

In the MHD setting, total pressure is defined as $p^* = p + \frac{1}{2} |\vec{B}|^2$.

Introducing dynamic magnetic fields to the hydrodynamic experiments allows for the study of the evolution of compound structures. The previous two model equations presented in Section 2.1.1 and Section 2.1.2 were described by a convex flux function, i.e., $F''(U)$ is strictly positive or negative. Their exact solutions are described by a Riemann fan where constant states are connected by single waves. The flux function for the ideal MHD equations is non-convex, and consequently, constant states can be connected by compound waves, e.g. a shock connected to the tail of a rarefaction wave [11].

2.2. Construction of flux-differencing schemes

The goal of FVM's is to numerically solve conservative systems as written in Eq.(3) [12, 13, 14, 15]. When Godunov first pursued solving the gas dynamic equations, he looked at the nonlinear flow in a 1D shock tube problem [16]. This consists of a discontinuous jump between two constant states and allows for the study of the evolution of two nonlinear waves (a shock and a rarefaction) and a contact discontinuity. Correctly predicting the interaction and propagation of nonlinear waves is the foundation of computational fluid dynamics.

Godunov approximated the flow by splitting the continuous profile into a large number of constant states and assuming piecewise constant states as an accurate solution at each cell. He immediately obtained cell edge values and the initial conditions for the Riemann problem by taking the piecewise constant

solution at the cell boundaries. By solving the Riemann problem and averaging the results in a conservative fashion, he computed the evolution of constant states exactly.
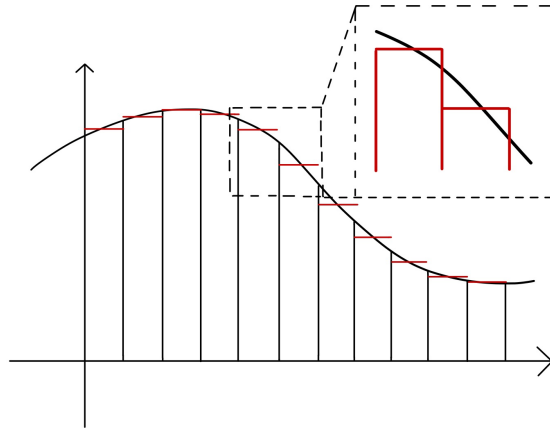
Figure 2: Godunov's discretization. A continuous profile is divided into a finite number of cells. The cell averaged quantity is the new cell value and initial condition to the Riemann problem.

Many high-order methods, such as the piecewise linear method (PLM) [17], the piecewise parabolic method (PPM) [18], the piecewise cubic method (PCM) [19], the weighted essentially non-oscillatory (WENO) methods [20, 21, 22, 23], and Gaussian Processes [24], are constructed in a similar fashion to advance cell-averaged quantities, $\bar{u}_j$, and predict nonlinear dynamics.

2.2.1. Finite volume discretization

For systems defined on $[x_0, x_m]$ for $t > 0$, the spatial domain is discretized such that $x_j = x_0 + j\Delta x$ for $j = 0, \ldots, m$, and the temporal domain is discretized such that $t^n = n\Delta t$ for $n \geq 0$. At $t = 0$, the system is defined as $u(x, 0) = u_0(x)$. For $t > 0$, $u_j^n = u(x_j, t^n)$ is defined at the center of each cell $I_j = [x_{j-\frac{1}{2}}, x_{j+\frac{1}{2}}]$. The following methods converge to a weak solution for a Courant number CFL < 1; and, the methods are stable, consistent, and have a conservative form if the numerical solution converges to a weak solution of the conservation law [12, 13, 15].

Consider a system with spatial discretization defining each cell value as the cell-averaged quantity, $\bar{u}_j^n$. The control volume in the space-time domain is defined as

$$[x_{j-\frac{1}{2}}, x_{j+\frac{1}{2}}] \times [t^n, t^{n+1}],\qquad(13)$$

and the cell-average quantity is obtained by integrating Eq.(3) over the control volume,

$$\bar{u}_j^n = \frac{1}{\Delta x} \int_{x_{j-\frac{1}{2}}}^{x_{j+\frac{1}{2}}} u(x, t^n) dx.\qquad(14)$$

See the appendix for more details.

2.2.2. Reconstruction polynomials

This section will describe the formulation of a spatially monotonic reconstruction polynomial,

$$p_j(x) = \sum_{k=0}^{n} c_k (x - x_j)^k,\qquad(15)$$

defined uniquely at each cell and used to construct the cell interface values. The degree of the polynomial, n, determines the spatial order of accuracy to be $n-1$. The polynomial must satisfy two constraints: $p_j(x)$ must be monotonic on I_j; and the new left and right states $u_{j\pm\frac{1}{2}}$ must lie between the neighboring volume-averaged quantities, i.e. $\bar{u}_{j-1}^n \leq u_{j-\frac{1}{2}}^n \leq \bar{u}_j^n$ and $\bar{u}_j^n \leq u_{j+\frac{1}{2}}^n \leq \bar{u}_{j+1}^n$. Once the unique polynomial is determined, the cell edge nodal values $u_{j-\frac{1}{2}}^n = p_j(x_{j-\frac{1}{2}})$ and $u_{j+\frac{1}{2}}^n = p_j(x_{j+\frac{1}{2}})$ are computed.

The leading constraint for the approximating polynomial is $\bar{p}_j^n = \bar{u}_j^n$, where

$$\bar{p}_j^n = \frac{1}{\Delta x} \int_{x_{j-\frac{1}{2}}}^{x_{j+\frac{1}{2}}} p(x, t^n) dx.\qquad(16)$$

By evolving integral quantities, Eq.(4) is constructed and the key property of FVM's is achieved. See the appendix for a more detailed derivation of a volume-averaged quantitiy and Eq.(4).

An nth-order spatial reconstruction polynomial requires n constraints to uniquely determine the n constants c_k. In the third-order PPM, the constants

$c_1, c_2,$ and c_3 in Eq.(15) are uniquely determined for the following conditions:

$$\begin{cases} \frac{1}{\Delta x} \int p_j(x) dx = \bar{u}_j^n, \\ p_j(x_{j-\frac{1}{2}}) = u_{L,j}^n, \\ p_j(x_{j+\frac{1}{2}}) = u_{R,j}^n. \end{cases} \qquad (17)$$

The approximate interface values, $u_{L;R,j}^n$, are computed in a separate step which constructs two fourth-order polynomials $\phi_\pm$ over four cells centered at $x_{j\pm\frac{1}{2}}$ that conserve cell average quantities.

$$\phi_\pm = \sum_{k=0}^{3} a_k^\pm (x - x_{j\pm\frac{1}{2}})^k \qquad (18)$$

The approximate left and right interface values are

$$u_{L,j}^n = \phi_-(x_{j-\frac{1}{2}}) = a_0^- \text{ and } u_{R,j}^n = \phi_+(x_{j+\frac{1}{2}}) = a_0^+ \qquad (19)$$

where

$$a_0^\pm = \frac{1}{2}(\bar{u}_{j-1+s}^n + \bar{u}_{j+s}^n) - \frac{1}{6}(\Delta\bar{u}_{j-1+s}^n - \Delta\bar{u}_{j+s}^n) \qquad (20)$$

with $s = 0$ for a_0^- and $s = 1$ for a_0^+. A complete derivation of the constants a_k can be found in most modern FVM textbooks [18, 25].

A total variation diminishing (TVD) slope limiter is a tool used for pursuing monotone preserving reconstruction profiles.

$$\Delta^{\text{TVD}}\bar{u}_j^n = \text{TVD}\left[\bar{u}_{j+1}^n - \bar{u}_j^n, \bar{u}_j^n - \bar{u}_{j-1}^n\right] \qquad (21)$$

In Section 4, new TVD methods are introduced and implemented to reduce oscillations near slowly moving shocks. For completeness, the minmod slope limiter and the original van Leer monotonized central difference (MC) limiter [26] are defined:

$$\Delta^{\text{TVD}}\bar{u}_j^n = \begin{cases} \text{minmod}\left(\frac{\bar{u}_j^n - \bar{u}_{j-1}^n}{\Delta x}, \frac{\bar{u}_{j+1}^n - \bar{u}_j^n}{\Delta x}\right), & \text{minmod}, \\ \text{minmod}\left(\frac{\bar{u}_{j+1}^n - \bar{u}_{j-1}^n}{2\Delta x}, 2\frac{\bar{u}_{j+1}^n - \bar{u}_j^n}{\Delta x}, 2\frac{\bar{u}_j^n - \bar{u}_{j-1}^n}{\Delta x}\right), & \text{MC limiter.} \end{cases} \qquad (22)$$

For two arguments, the minmod function returns zero if a new local extremum is created (i.e. the left and right states are opposite signs), otherwise it returns

the value of lesser magnitude.

$$\text{minmod}(u_L, u_R) = \begin{cases} u_L & \text{if } |u_L| < |u_R| \text{ and } u_L u_R > 0, \\ u_R & \text{if } |u_R| < |u_L| \text{ and } u_L u_R > 0, \\ 0 & \text{if } u_L u_R < 0. \end{cases} \tag{23}$$

2.2.3. Characteristic tracing

To achieve second-order accuracy in time, the edge values $u_{L;R,j}^n$ are advanced by $\Delta t/2$ yielding $u_{L;R,j}^{n+\frac{1}{2}}$. This is done by averaging the solution over $[t^n, t^{n+1}]$, where the solution at t^{n+1} is calculated by tracing characteristics back in time to the known solution at t^n. The new temporally evolved and spatially averaged values at the half-time step, $u_{L;R,j}^{n+\frac{1}{2}}$, will be used as the initial conditions to the Riemann problem to compute numerical fluxes $\hat{F}_{j\pm\frac{1}{2}}^{n+\frac{1}{2}}$ in Eq.(4).

Eq.(3) is rewritten as

$$\frac{\partial U}{\partial t} + \frac{\partial F}{\partial U}\frac{\partial U}{\partial x} = 0. \tag{24}$$

Since the system is hyperbolic, by definition the Jacobian matrix $\frac{\partial F}{\partial U}$ can be reduced to a diagonal matrix with real entries $\lambda^{(k)}$ for each kth wave.

$$\frac{\partial F}{\partial U} = R\Lambda L \tag{25}$$

Eq.(25) is a singular value decomposition of the Jacobian matrix into the product of R, a square matrix whose columns are the right eigenvectors $\vec{r}^{(k)}$, Λ, a diagonal matrix consisting of the eigenvalues $\lambda^{(k)}$, and L, a square matrix whose rows are the left eigenvectors $\vec{l}^{(k)}$. Let $w^{(k)}(x,t)$ be the kth wave characteristic variable and k^{th} entry of vector W. Then, the characteristic variables can be written

$$W = R^{-1}U = LU, \tag{26}$$

and the conservative formulation is rediscovered by projecting $w^{(k)}$ to the conservative space,

$$u(x,t) = \sum_{k=1}^{m} \vec{r}_k w^{(k)}(x,t). \tag{27}$$

11

The eigenvector projection reduces the coupled nonlinear system to a decoupled system of linear advection equations in terms of the characteristic variables, $W_t + \Lambda W_x = 0$. For each kth wave and each cell j, the problem reduces to

$$\frac{\partial w_j^{(k)}}{\partial t} + \lambda_j^{(k)} \frac{\partial w_j^{(k)}}{\partial x} = 0. \tag{28}$$

The eigenvalue $\lambda_j^{(k)}$ of the Jacobian matrix is the characteristic speed of the kth wave at cell j.

The exact solution to the system of linear advection equations is a family of characteristic lines. The solution to each equation is self-similar, i.e. $w(x,t) = w(x/t)$. Consequently, the characteristic line can be used to predict the solution at future time as long as no shock emerges. The exact solution of the edge value at the next time step, $w(x_{j+\frac{1}{2}}, t^{n+1})$, is found by considering each kth characteristic at t^n that reaches the cell interface in time Δt. As derived in the appendix, the explicit solution for the mth component of the right half-time step is

$$v_{R,j:m}^{n+\frac{1}{2}} = \sum_{k; \lambda_j^{(k)} > 0} \frac{1}{\lambda_j^{(k)} \Delta t} \int_{x_{j+\frac{1}{2}} - \lambda_j^{(k)} \Delta t}^{x_{j+\frac{1}{2}}} \vec{r}_{j:m}^{(k)} \vec{l}_j^{(k)} \cdot \vec{p}_j(x) dx. \tag{29}$$

A similar solution exists for the left half-time step, and establishes the initial conditions for the Riemann problem at each interface $x_{j\pm\frac{1}{2}}$.

2.2.4. The Riemann problem

After discretizing the domain and building reconstruction polynomials, the dispersive flux term, $\hat{F}_{\text{diff}}$, is calculated by solving the Riemann problem at each cell boundary. The initial condition for the Riemann problem consists of two states connected by a single jump satisfying the Rankine-Hugoniot jump condition $\Delta F = S\Delta U$, which states the change in flux is proportional to the change in state according to the shock speed S. At $t = 0$, the left half of the domain takes constant value U_L and the right half of the domain takes constant value U_R.

$$u(x,0) = \begin{cases} U_L, & x < 0 \\ U_R, & x > 0 \end{cases} \tag{30}$$

The exact solution is a set of nonlinear waves and leads to a set of nonlinear algebraic equations. Pursuing the exact solution at each cell interface is computationally expensive because it generally involves an iterative method. The original first-order Godunov's method computes the exact solution with $U_L = U_j$ and $U_R = U_{j+1}$ [16], and modern methods devise means of approximating the nonlinear wave interaction.

For example, Roe's method [27] finds an approximate Jacobian matrix, $\tilde{A}(U_L, U_R)$, to compute

$$\hat{F}_{\text{diff}} = -\frac{1}{2}\tilde{A}\Delta U. \tag{31}$$

The average Jacobian flux matrix must satisfy the following three conditions: $\tilde{A}$ has a set of real eigenvalues and right eigenvectors, and $\tilde{A}(U,U) = \frac{\partial F}{\partial U}$, and $\tilde{A}$ is conservative across discontinuities, i.e.

$$F(U_R) - F(U_L) = \tilde{A}(U_R - U_L). \tag{32}$$

The flux function of Roe is then defined as

$$\hat{F}_{\text{diff}} = -\frac{1}{2}\sum_k l^{(k)}|\lambda^{(k)}|r^{(k)} \cdot (U_R - U_L). \tag{33}$$

On the other hand, Osher's scheme [28, 29, 30] considers a path integral Γ in state space uniquely determined by the Riemann problem,

$$\hat{F}_{\text{diff}} = -\frac{1}{2}\int_{U_L}^{U_R} \frac{\partial F}{\partial U} dU = -\frac{1}{2}\sum_{k=1}^{K} \cdot \int_{\Gamma^{(k)}} r^{(k)}\lambda^{(k)} d\alpha^{(k)} \tag{34}$$

The initial condition of the characteristic variable $w^{(k)}$ determines the characteristic variable $\alpha^{(k)}$. The appropriate linear sum of $\alpha^{(k)}$'s rediscovers the conservative form, i.e.

$$U_L = \sum_k \alpha^{(k)}r^{(k)}, \qquad U_R = \sum_k \beta^{(k)}r^{(k)}. \tag{35}$$

The original Osher-Solomon method requires calculating solutions within each characteristic field, and an additional sonic point for genuinely non-linear fields. Dumbser and Toro [31] choose to integrate along a line segment Ψ split at points

13

s_j with appropriate weights w_j according to a Gauss-Legendre quadrature rule of size G. The effectiveness of the universal Osher Riemann solvers given by

$$\hat{F}_{\text{diff}} = -\frac{1}{2} \left(\sum_{j=1}^{G} \omega_j |A(\Psi(s_j))| \right) (U_R - U_L).　\qquad (36)$$

will be presented in Section 5. See appendix for more details on the construction of Eq.(36).

3. Slowly moving shocks

Since it was first observed by Woodward and Collela in 1984 [1], many practitioners have studied the error generated by slowly moving shocks. In this section, I will address each of these case studies and build a working framework to analyze the problem mathematically.

3.1. History

When presenting their construction of PPM [18], Woodward and Colella observed low-amplitude post-shock oscillations were produced when the speed of the shock became small relative to the upwind flow speed. In the companion paper, the authors presented a detailed discussion of strong-shock calculations using 2-dimensional difference schemes for compressible hydrodynamics [1]. Three approaches were proposed to address post-shock oscillations: introducing artificial viscosity, using a linear hybridization of high- and low-order accurate flux functions, and pursuing nonlinear solutions to Riemann's problem. The first approach smears the sharp shock over multiple cells by adding viscosity and heat diffusion to the system. In the second approach, using high-order methods in smooth flows and low-order methods near discontinuities captures a sharp discontinuity with minimal oscillations by utilizing the diffusive properties of low-order methods. The authors stated that since the wavelength of the oscillations are many cells wide, the error due to such oscillations cannot be sufficiently dampened by the second approach. The third approach, pursuing nonlinear solutions to Riemann's problem, implies the use of Godunov's method

[16] and conservation laws. As discussed in Section 2.2, the use of interpolation polynomials, characteristic tracing and approximate Riemann solvers is computationally complex. However, the authors showed that the explicit nonlinearity of Godunov's method can achieve accurate results for smooth flows and narrow structures.

The next major study, conducted by Roberts [5], analyzed the internal structure of the discrete shock and discussed the discrepancy between the numerical shock structure and the exact shock curve. Roberts examined performances of the first order Godunov method, Roe's flux function, and Osher's flux function in flows containing a slowly moving shock, or flows where the ratio of the shock speed to the maximum wave speed in the domain is $\sim 1/50$. He claimed the discrete shock solution must lie exactly on the shock curve in order to eradicate the production of oscillations. He supported his argument by noting the success of Osher's flux function, a method that calculates the intercell flux by considering an integral path in phase space. Unlike the Roe or Godunov schemes which recognize shocks if the Rankine-Hugoniot condition is satisfied, Osher's scheme is formulated in such a way that left and right states of a shock are connected by a compound simple wave path. Therefore, through Osher's formulation, no two states are connected by a shock, more of the internal structure is preserved, and the discrete shock structure lies closer to the Hugoniot curve. In the scalar case, such as Burgers' equation, there can be a 1-shock connecting the left and right states. This satisfies Roberts condition for no oscillations, and as will be seen in Figure 3, there are no upwind running waves produced at the slowly moving shock.

Billet and Toro [4] addressed the loss of monotonicity behind slowly moving shocks. They supported the previously constructed argument that the dissipation in Godunov's scheme is proportional to the wavespeed. Near slowly moving or nearly stagnant shocks, this speed is necessarily very small, and consequently, there is insufficient dissipation to remove the erroneous oscillations. Their proposed solution is to identify the location of the slowly moving shock and in that localized region use a low-order method. In order to identify the location of the

15

slowly moving shock, Billet and Toro constructed a shock parameter G, which will be defined in Section 3.2. Their explicit definition is useful for identifying the locations of slowly moving shocks, but post-shock oscillations are not generated solely by slowly moving shocks. Rather, slower shocks produce longer wavelength and larger amplitude oscillations. Similarly, it can be shown that higher frequency oscillations are generated by increasing the grid resolution.

Focusing on slow or steady shocks in the Euler equations, Jin and Lui [6] studied the effects of unsteady numerical viscosity. Their analysis emphasized the initial spike in the momentum profile and the upwind running waves that carry mass to compensate for the spike and conserve momentum. It is noted that the periodicity of the momentum peaks are related to the solution of a traveling wave and the time it takes for the shock to cross a grid cell. The shock profile is not continuously defined within each period and is unsteady. The authors pointed to this as the source of downstream waves and the polluted solution for all future time. They proposed the use of systematically monotone, TVD, or essentially non-oscillatory methods.

Arora and Roe [3] studied post-shock oscillations by comparing the performance of the first order Godunov method, Roe's flux function, and Osher's flux function. They determined that a period of a slowly moving shock's oscillations are approximately equal to the time T it takes for the shock to cross a cell

$$T = \frac{\Delta x}{|S|}, \tag{37}$$

where Δx is the size of the mesh spacing and S is the speed of the shock. The wavelength of the oscillation is $\lambda_0 = \left| \frac{\lambda \Delta x}{S} \right|$ where λ is the speed of the wave carrying downwind oscillations. Clearly, decreasing the shock speed will increase the wavelength of the error. A change in sign of the wavespeed associated with the shock will necessarily expose the strength of the weaker waves not associated with the shock. However this does not restrict the error to such flows; they observed that fast shocks exhibited the same error with much smaller effects. The authors claimed the root cause of the error is that numerical schemes solving the Riemann problem produce a full set of *multiple* waves of non-zero

16

strength, all of which contribute wave properties (i.e. oscillations) that travel with different non-zero wave speeds. However, a mathematically valid solution should require only a *single* shock wave moving between the left and right states of the shock along the Hugoniot curve, which is not the case for general nonlinear systems. According to the authors' argument, systems with linear or monotone Hugoniot curves will not produce oscillations. The authors concluded that there is no complete cure to the problem, and proposed the Osher flux function as one suitable means of reducing the error.

Karni and Canic [2] study the modified equations of two first-order finite difference methods displaying different behaviors in phase space and in the post-shock region. The first method experiences vanishing viscosity near the discontinuity at which point lower order terms get activated as they are comparable in strength. This approach disrupted the solution and was not successful. The better behaved second method was considered as a traveling wave solution to a modified equation of the numerical scheme. While there was a close agreement between the numerical orbit of a fast shock and the traveling wave solution, the numerical orbit of a slow shock did not display the same properties. It was found to have a low order source term inside the shock layer. This term projected a perturbation onto the cross characteristic wave families, where solutions to the fast shock remained tangent to the shock characteristics.

Stiriba and Donat observed noise in the first time steps of a shock calculation and the immediate deviation of the numerical orbit from the Hugoniot curve [9]. This is a result of the solution of the Riemann problem generating a full set of waves in all characteristic fields within the shock layer. The authors achieved a first-order accurate scheme by considering the local propagation of characteristics in the construction of an intermediate state to be used in the flux function. By building a flux function in such a fashion, the authors successfully dampened post-shock oscillations.

Sikolis et. al. [8, 32] investigated the discrete shock structure computed by a variety of high resolution shock capturing schemes. While they successfully eliminated first-order error in a 2×2 system by introducing a viscosity matrix,

they did not claim to have built a robust solution for future slowly moving shock capturing schemes. They studied the modified equation derived through Taylor series expansions, and as was observed in earlier studies, the phase plots of the modified equations at a slow shock deviated significantly from the exact shock curve. Because they observed different behavior in post-shock regions for modified equations with similar phase plots, the authors suggested that studying numerical phase space orbits is not the best tool for addressing discrete shock structures.

The most recent study of slowly moving shocks by Johnsen et. al. [7, 33, 34] described means of controlling the artificial viscosity coefficients to ensure sufficient numerical dissipation. The error was divided into two types: a start-up error associated with the initial momentum spike, and the subsequent unphysical post-shock oscillations. The authors reduced downstream oscillations by enforcing a lower limit on the wavespeed associated with the wave crossing the shock and reduced the effect of cross characteristic waves perturbing the solution. Bounding the wavespeed is a powerful technique for introducing diffusion to the numerical scheme [10].

3.2. A formal definition

In this section a formal definition is presented for the existence of a slowly moving shock based on a shock parameter comparing upwind and downwind characteristics associated with the shock. The definition was introduced by Billet and Toro [4].

A k-shock exists between the left state u_j, and right state u_{j+1}, if the shock speed is intermediate to the eigenvalues, in the following fashion:

$$\lambda_{j+1}^{(k)} < S < \lambda_j^{(k)}, \text{ and} \tag{38}$$

$$\lambda_j^{(k-1)} < S < \lambda_{j+1}^{(k+1)}. \tag{39}$$

Let $\lambda_L = \lambda_j^{(k)}$ and $\lambda_R = \lambda_{j+1}^{(k)}$, then for a wave with a k-shock and positive shock speed $S > 0$:

$$1 > \frac{S}{\lambda_L} > \frac{\lambda_R}{\lambda_L} \equiv G. \tag{40}$$

18

And for a wave with a k-shock and negative shock speed $S < 0$:

$$1 > \frac{S}{\lambda_R} > \frac{\lambda_L}{\lambda_R} \equiv G. \tag{41}$$

The shock parameter G is defined as

$$G \equiv \frac{\lambda_{\text{downwind}}}{\lambda_{\text{upwind}}} \tag{42}$$

and a slowly moving shock exists between the left and right state if $G < 0$.

This is a strict definition that is rarely met in numerical experiments, and fortunately, unnecessary to meet in order to study post-shock oscillations. Instead of enforcing $G < 0$, previous studies restrict the shock parameter to $G \ll 1$ for identifying slowly moving shock regions [33]. This restriction satisfies a similar definition stated by previous studies, i.e., a slow shock exists if the ratio of shock speed to maximum wave speed is close to zero or negative [3, 5].

4. Modern slope limiters

The literature has mixed reviews on the effectiveness of high-order accurate TVD slope limiters for reducing post-shock oscillations. Roberts [5] and Jin & Lui [6] claim the use of TVD concepts accentuate the error. Roberts demonstrated that the use of the 'minmod' slope limiter preserves the downstream oscillations for a longer distance. More importantly, he argued the TVD property only applies to scalar equations and is completely dependent on the underlying low-order scheme being truly monotone. In contrast, Striba & Donat [9] argued that high-order schemes using TVD and ENO logic to extend low-order methods do not necessarily amplify or preserve the oscillations. They implemented an ENO piecewise polynomial reconstruction [35] and achieved similar results to Roberts and Jin & Lui. In another simulation employing the piecewise hyperbolic method, an extension of an ENO-type reconstruction introduced by Marquina [36], the author saw a significant improvement in the treatment of post-shock oscillations. They concluded the use of TVD and ENO methods do not necessarily amplify or preserve the oscillations.

In this section, an upwind-biased slope limiter [37] and a new slope limiter that calculates a fourth-order approximation of the slope are introduced. The two methods define the flux limiter Δ^{TVD} formulation to be used in the PPM construction of the left and right Riemann states, i.e. (u_L, u_R). In PPM, the pair (u_L, u_R) is given as Eq.(43), which are fourth-order accurate interface values and used in the Riemann problem to compute upwind fluxes.

$$
\begin{aligned}
u_L &= \frac{1}{2}(\bar{u}_{j-1} + \bar{u}_j) + \frac{1}{6}(\Delta^{\text{TVD}}\bar{u}_{j-1} - \Delta^{\text{TVD}}\bar{u}_j) \\
u_R &= \frac{1}{2}(\bar{u}_j + \bar{u}_{j+1}) + \frac{1}{6}(\Delta^{\text{TVD}}\bar{u}_j - \Delta^{\text{TVD}}\bar{u}_{j+1})
\end{aligned}
\tag{43}
$$

Here, Δ^{TVD} is any conventional slope limiter such as MC, minmod, or van Leer.

The first method studied is an upwind-biased slope limiter [37]. This scheme places greater emphasis on upwind information in an attempt to maximize the strength of the shock characteristic and minimize the strength of the downwind running characteristic families. The second slope limiter considers a high-order approximation of the slope at the shock using WENO-type logic. This method considers a fourth-order approximation of the slope derived during the construction of the piecewise cubic method [19], a fourth-order reconstruction method.

4.1. Upwind-biased slope limiter

The post-shock oscillations are a product of upwind running waves of non-vanishing strength that are not associated with the shock wave. To reduce the strength of these waves, Lee favored upwind information in slope limiting calculations [37]. The upwind-biased slope limiter formulation is as follows:

$$
\Delta^{\text{up}}u_i = \begin{cases}
\Delta^{\text{TVD}}u_{i-1}, & \text{if } u_x > 0, \\
\Delta^{\text{TVD}}u_i, & \text{if } u_x = 0, \\
\Delta^{\text{TVD}}u_{i+1}, & \text{if } u_x < 0.
\end{cases}
\tag{44}
$$

The new upwind-biased slope limiter is employed locally at cells that are tagged as slowly moving shock cells. A cell is detected as a slowly moving shock if there is a change in sign of the eigenvalue associated with the shock wave across either of the cell boundaries of the jth cell. At cell j, define λ_j^{SL} as the characteristic

speed of the left-going shock and λ_j^{SR} as the characteristic speed of the right-going shock. Then, upwinding is implemented if any of the three following conditions are met:

$$1. \ \lambda_{j-1}^{\text{SR}} > 0 \text{ and } \lambda_{j+1}^{\text{SL}} < 0, \text{ or} \tag{45}$$

$$2. \ \lambda_{j-1}^{\text{SR}} > 0 \text{ and } \lambda_{j}^{\text{SL}} < 0, \text{ or} \tag{46}$$

$$3. \ \lambda_{j}^{\text{SR}} > 0 \text{ and } \lambda_{j+1}^{\text{SL}} < 0. \tag{47}$$

Numerically speaking, one of these conditions is met so long as the solution is not a pure rarefaction wave. As illustrated in the Section 5, introducing this bias increases numerical dissipation and reduces the strength of the oscillations.

4.2. WENO-type slope limiter

PCM [19] can be thought of as an extension of combining PPM and WENO-JS [21]. The method yields a fourth-order accurate method by considering a cubic piecewise reconstruction polynomial on each cell. In order to determine the unique reconstruction polynomial at each cell, an additional constraint is required to calculate the constant c_3 in the third-degree polynomial

$$p_j(x) = c_0 + c_1(x - x_j) + c_2(x - x_j)^2 + c_3(x - x_j)^3. \tag{48}$$

As shown in [38], the constant is determined to be

$$c_3 = \frac{4}{\Delta x^3} \left(u_{R,j} - u_{L,j} - \Delta x u'_{c,j} \right), \tag{49}$$

where the left and right Riemann states, $u_{R,j}$ and $u_{L,j}$, are determined using the standard WENO build [35, 20, 39, 23], which achieves fifth-order accurate spatial reconstruction with sharp shock transitions. The undetermined value, u'_j, is a fourth-order accurate approximation of the slope at cell j and a natural link to constructing a new slope limiter.

A WENO-type reconstruction method is used to approximate $u'(x_j, t^n)$. The process begins with building two third-degree polynomials defined on a five point stencil centered around cell j:

$$\phi_{\pm}(x) = \sum_{k=0}^{3} a_k^{\pm} (x - x_{j\pm\frac{1}{2}})^k. \tag{50}$$

21

The constants $a_k^{\pm}$ are determined by maintaining volume averaged quantities on each cell as written in Eq.(51) and Eq.(52), and uniquely determine the polynomials $\phi_{\pm}$.

$$\frac{1}{\Delta x} \int_{I_k} \phi_-(x)dx = \bar{u}_k^n, \qquad \text{for } j - 2 \leq k \leq j + 1 \tag{51}$$

$$\frac{1}{\Delta x} \int_{I_k} \phi_+(x)dx = \bar{u}_k^n, \qquad \text{for } j - 1 \leq k \leq j + 2 \tag{52}$$

Taking their derivatives and the linear constant weights $\gamma_{\pm} = 1/2$ provides a scheme for the construction of the approximate derivative,

$$u_j' = \gamma_- \phi_-'(x_j) + \gamma_+ \phi_+'(x_j), \tag{53}$$

however linear weights produce oscillatory behavior. To achieve a non-oscillatory scheme, nonlinear weights $w_{\pm}$ are computed based on the smoothness of polynomials $\phi_{\pm}$ over their respective four cell stencils. See [20] for details of derivations of the linear and nonlinear weights.

The smoothness indicators $\beta_{\pm}$ are defined as

$$\beta_{\pm} = \sum_{s=2}^{3} \left(\Delta x^{2s-1} \int_{I_j} \left[\frac{d^s}{dx^s} \phi_{\pm}(x) \right]^2 dx \right). \tag{54}$$

The nonlinear weights are then defined as

$$w_{\pm} = \frac{\tilde{w}_{\pm}}{\tilde{w}_- + \tilde{w}_+} \tag{55}$$

where

$$\tilde{w}_{\pm} = \frac{\gamma_{\pm}}{(\epsilon + \beta_{\pm})^m}, \qquad\qquad \text{for WENO-JS} \tag{56}$$

$$\tilde{w}_{\pm} = \gamma_{\pm} \left(1 + \left(\frac{|\beta_+ - \beta_-|}{\epsilon + \beta_{\pm}} \right)^m \right), \qquad \text{for WENO-Z.} \tag{57}$$

Here, ϵ is a very small positive number introduced to eliminate the chance of dividing by zero. In smooth flows, β's are small and the nonlinear weights are equivalent to the linear weights. Flows with sharp discontinuity produce large β's, and the nonlinear weights approach zero so long as the other polynomial is relatively smooth.

A linear combination of candidate slopes is considered in Eq.(58) and the weight to each is a nonlinear function of the grid values based on local smoothness determined by Eq.(54). The fourth-order accurate approximation of the slope u'_j is

$$u'_j = w_- \phi'_-(x_j) + w_+ \phi'_+(x_j).$$ (58)

An undivided slope limiter is constructed based on the approximate slope in Eq.(58):

$$\Delta^{\text{weno}} u_j \approx \Delta x \frac{\partial u(x_j, t^n)}{\partial x_j} \approx \Delta x u'_j.$$ (59)

In Section 5, the performance of the WENO-type slope limiter in the HD slow shock experiment and in the Brio-Wu MHD shock tube is demonstrated. It achieves accurate solutions similar to the slope limiters of minmod, MC, and van Leer, but with greater computational complexity.

5. Results

In this section numerical experiments and results are presented. A variety of experiments for hydrodynamics and magnetohydrodynamics are performed in which the codes ability to capture smooth and discontinuous flows is tested. Upwinding with PPM [18] and the universal Osher Riemann [31] solver will be compared with the fifth-order WENO-Z method [23] computed with RK4 temporal advancement to provide an accurate solution in space and time. A courant number of CFL $= 0.8$ was used in all of the simulations.

5.1. Burgers' equation

The first numerical experiment considers a left-going slowly moving shock in the Burger's equation. This experiment was designed by Billet and Toro [4] to produce a shock with speed $S = -0.02$.

$$u = \begin{cases} 0.96 & \text{if } x < 0.5, \\ -1.0 & \text{if } x > 0.5 \end{cases}$$ (60)

For scalar equations, any two states U_L and U_R can be connected by a single wave. Consequently, internal shock points are computed exactly and no downstream running waves pollute the solution, as is the case with systems of equations. This is demonstrated in Figure 3.
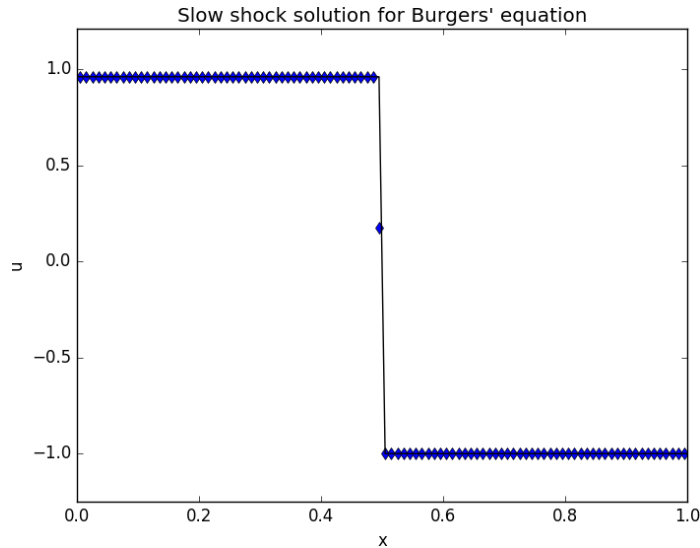

Figure 3: The slowly moving shock problem for the scalar Burger's equation at $t = 0.2$ using PLM with the MC slope limiter. The numerical solution is plotted with the analytic solution.

5.2. Hydrodynamics

5.2.1. Sod's shock tube

Sod's shock tube problem [40] is studied to observe the numerics ability to capture a shock, rarefaction, and contact discontinuity. This problem sets up an initial left and right state with high density and pressure on the left half of the domain.

$$(\rho, u, p) = \begin{cases} (1, 0, 1) & \text{if } x < 0.5, \\ (0.125, 0, 0.1) & \text{if } x > 0.5 \end{cases} \tag{61}$$

The experiment takes outflow boundary conditions, a ratio of specific heats $\gamma = 1.4$, and is observed at $t = 0.2$. As illustrated in Figure 4, a shock, rarefaction, and contact discontinuity evolve from the initial boundary of the

24

two states. Figure 4b shows a zoom-in on the oscillations behind the right-running contact discontinuity. Upwinding and the WENO-type slope limiter accurately capture the physics and may lead to an improved solution.
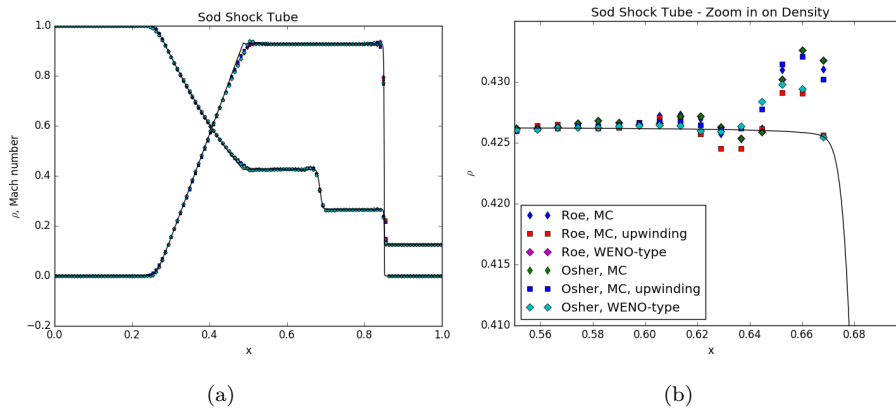

(a)   (b)

Figure 4: Sod's shock tube problem at $t = 0.2$ computed with PPM on a grid size of $N = 128$. (a) Density and Mach number are plotted for the Roe and Osher Riemann solvers with and without upwinding. (b) A zoom in on the shock front in the density profile exposes minor oscillations are produced behind the contact discontinuity. The WENO-Z with RK4 experiment was calculated on a grid size of $N = 2048$ and is a close approximation to the analytic solution.

5.2.2. The Shu-Osher problem

The next numerical test is the Shu-Osher problem [41]. This problem consists of initializing a Mach 3 shock wave at -4.0 on the domain $[-4.5, 4.5]$. As the shock propagates across the domain it encounters small sinusoidal perturbations in a nearly constant density field. Two post-shock wave sets are produced with one set having twice the frequency of the other. The experiment takes a ratio of specific heats of $\gamma = 1.4$ and outflow boundary conditions, and is observed at $t = 1.8$.

$$(\rho, u, p) = \begin{cases} (3.8571, 2.6293, 10.3333) & \text{if } x < -4.0, \\ (1 + 0.2\sin(5x), 0, 1) & \text{if } x > -4.0 \end{cases} \quad (62)$$

The results for Roe, Roe with upwinding, Osher, and Osher with upwinding are computed with PPM and the MC slope limiter on a a grid size of $N = 256$.

The results for WENO-Z with RK4 are computed with the MC slope limiter on a grid size of $N = 2048$. As illustrated in Figure 5, upwinding has little effect on the code's ability to capture the shock and high-frequency density perturbations.

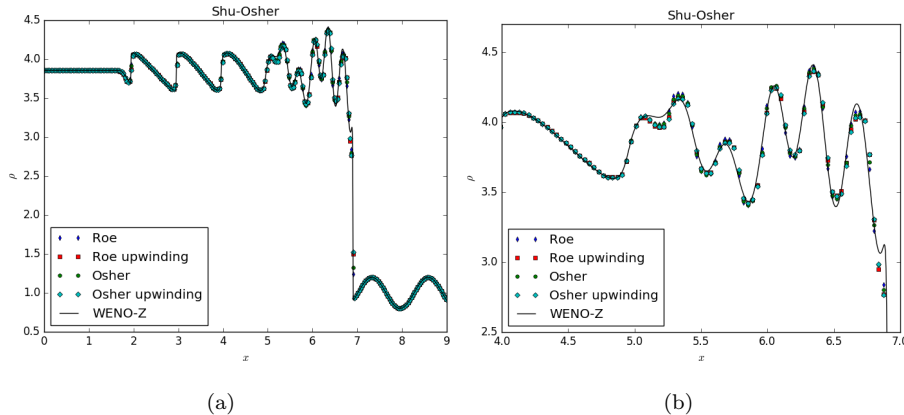(a)   (b)

Figure 5: The Shu-Osher problem at $t = 1.8$. The experiments are computed with PPM and MC slope limiter on $N = 256$ and compared to WENO-Z with RK4 on $N = 2048$.

5.2.3. Two-blast

By creating a pocket of low pressure between two regions of high pressure, the two-blast experiment produces strong shocks and discontinuities [1].

$$
(\rho, u, p) = \begin{cases} (1, 0, 1000) & \text{if } x < 0.1 \\ (1, 0, 0.01) & \text{if } 0.1 < x < 0.9, \\ (1, 0, 100) & \text{if } x > 0.9 \end{cases} \tag{63}
$$

In Figure 6, the results for upwinding in the HLL and universal Osher Riemann solvers at $t = 0.38$ are presented. It is evident the Osher solver out performs the HLL solver, however, upwinding does not necessarily achieve a more accurate solution. The density spike at $x = 0.8$ is closer to the high-resolution WENO-Z solution, but the solvers without upwinding maintain a sharper spike at $x = 0.65$. It is expected that the low-resolution experiments do not maintain as sharp of peaks as the WENO-Z solution in Figure 6.
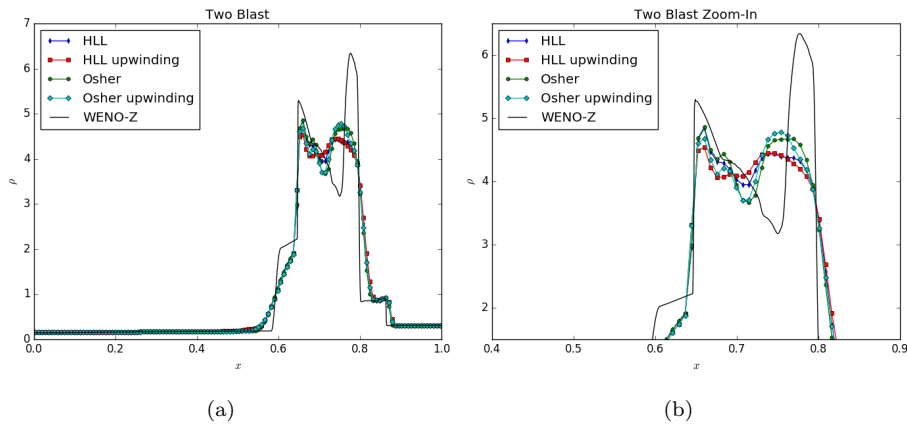
26

Figure 6: The two-blast problem at $t = 0.038$. The HLL and Osher Riemann solvers are used in conjunction with the MC slope limiter with a grid size of $N = 128$. The high-resolution solution was computed with the HLLC Riemann solvers with the MC slope limiter on a grid size of $N = 1024$.

5.2.4. Slow shock problem

The following slow shock experiment, introduced by Roberts [5] and repeated by Billet & Toro [4], is designed to produce a left-running slow shock with speed $S = -0.03$. The right state is obtained from the Rankine-Hugoniot jump condition and by enforcing $a = 1.0$ across the domain.

$$(\rho, u, E) = \begin{cases} (1, 3, 6.2858) & \text{if } x < 0.5 \\ (9.4864, 0.2446, 17.2238) & \text{if } x > 0.5 \end{cases} \tag{64}$$

The experiment takes outflow boundary conditions and a ratio of specific heats $\gamma = 1.4$, and is observed at $t = 0.1$. In Figures 7a and 7c, large amplitude oscillations are seen behind the slowly moving shock front in density, velocity, and pressure. Once upwinding is applied, there is successful dissipation of the error in all three state variables as evident in Figure 7b and Figure 7d. The performance of the WENO-type slope limiter is demonstrated to be comparable to standard TVD slope limiting methods in Figure 8. It is further illustrate in Figure 9 that upwinding effectively introduces numerical dissipation in regions of slowly moving shocks and achieves a more accurate solution.
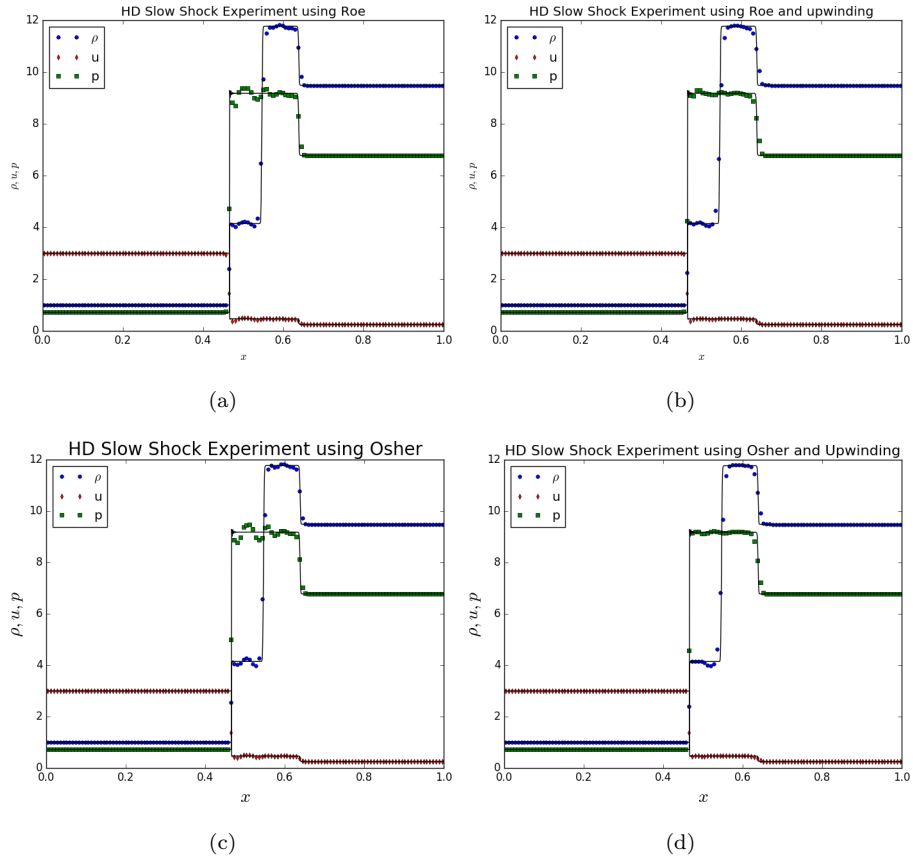
27

Figure 7: The slowly moving shock problem for the full Euler equations at $t = 0.1$. The solution for (a) Roe, (b) Roe with upwinding, (c) Osher, and (d) Osher with upwinding are computed on a grid size of $N = 128$ with PPM and the MC slope limiter. These results are compared to WENO-Z computed with RK4 on a grid size of $N = 2048$.
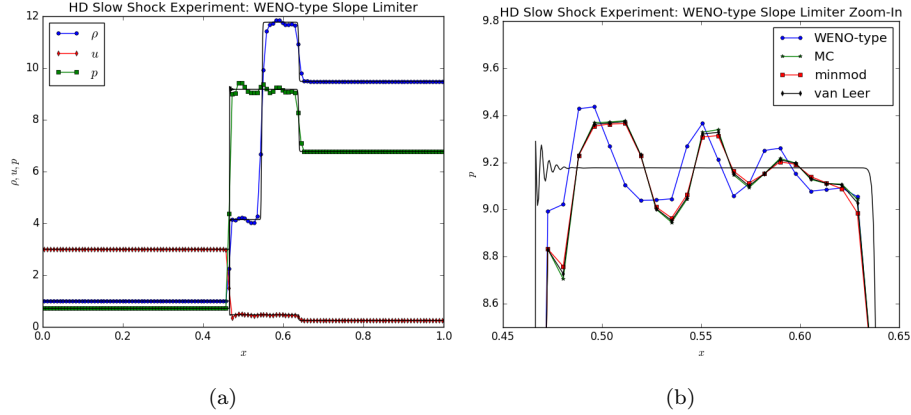
Figure 8: (a) The performance of the WENO-type slope limiter is presented in the hydrodynamics slow shock experiment with PPM and Roe on a grid size of $N = 256$. (b) A zoom-in on the oscillations in pressure for the slope limiters of WENO-type, MC, minmod, and van Leer exposes a shift in the location of the oscillations for the new slope limiter.

5.3. Magnetohydrodynamics

5.3.1. MHD shock tube

Next, a simple MHD shock tube experiment introduced by Ryu et. al. [11] is studied to confirm our codes ability to capture all MHD wave structures. The initial conditions are

$$
(\rho, u_x, u_y, u_z, B_y, B_z, p) = \begin{cases} (1.08, 1.2, 0.01, 0.5, 1.01554, 0.564189, 0.95) \\ \qquad \text{if } x < 0.5, \\ (1, 0, 0, 0, 1.128379, 0.564189, 1) \\ \qquad \text{if } x > 0.5. \end{cases}
\tag{65}
$$

The experiment takes a ratio of specific heats $\gamma = 1.6666$ and is observed at $t = 0.2$. Figure 10 shows the presence of a contact discontinuity, left- and right-going fast shocks, and left- and right-going slow shocks. It is interesting to note upwinding does not maintain as sharp of features, rather, it effectively introduces more artificial viscosity.

29
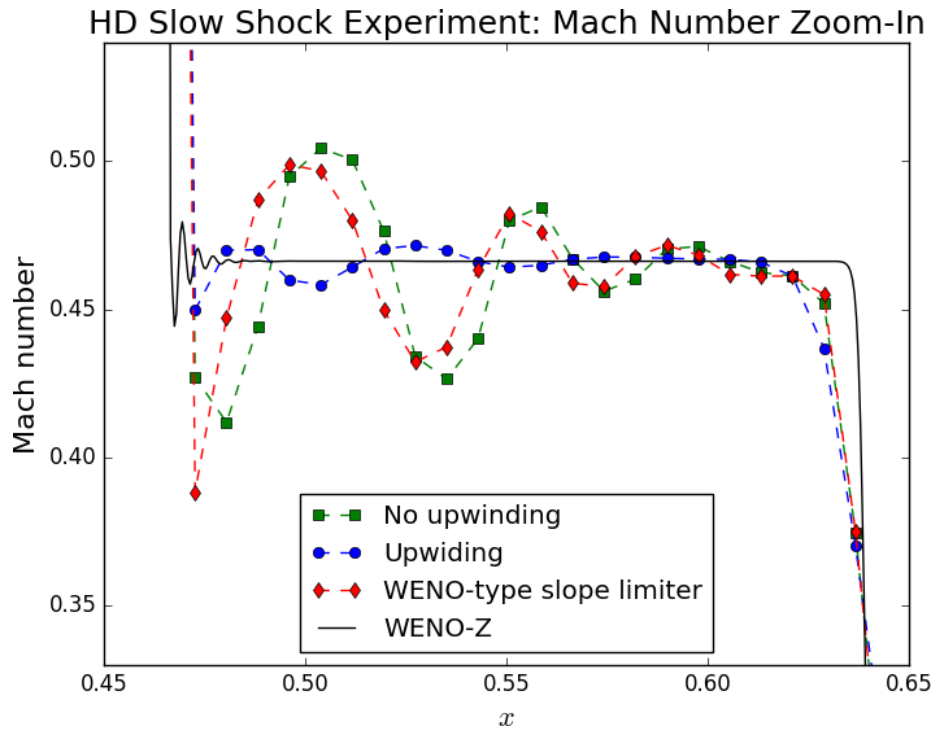
Figure 9: A zoom-in on the oscillations in the hydrodynamics slow shock experiment observed at $t = 0.1$. The experiments were computed with the universal Osher Riemann solvers on a grid size of $N = 128$ with the MC slope limiter (green and blue) and the WENO-type slope limiter (red). The high-resolution solution is computed with WENO-Z, RK4, and a grid size of $N = 2048$.
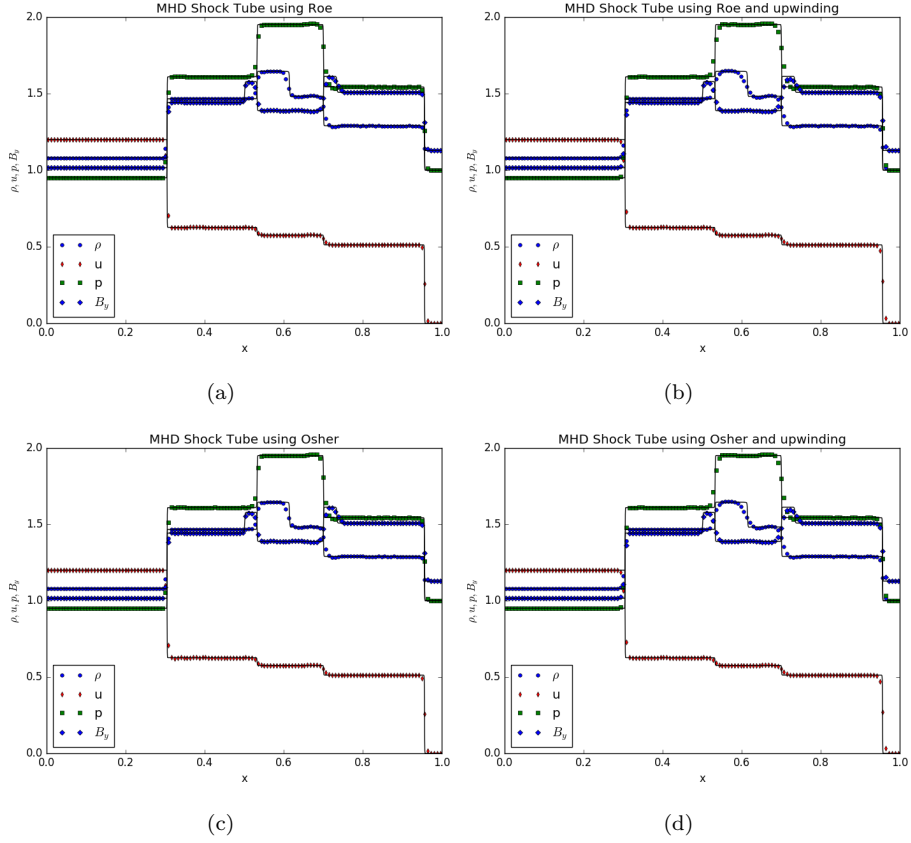
Figure 10: The MHD shock problem at $t = 0.2$. Solutions are computed with the Riemann solvers of (a) Roe, (b) Roe with upwinding, (c) Osher, (d) Osher with upwinding. PPM and the MC slope limiter are used on a grid size $N = 128$. The high-resolution solution is computed with WENO-Z and RK4 on a grid size $N = 2048$.

5.3.2. Brio-Wu MHD shock tube

The Brio-Wu shock tube problem [42] is studied to test the numerics ability to capture compound structures and reduce oscillations near a slowly moving shock in MHD. The initial Riemann problem has the left and right states

$$(\rho, u_x, u_y, u_z, B_y, B_z, p) = \begin{cases} (1, 0, 0, 0, 1, 0, 1) & \text{if } x < 0.5, \\ (0.125, 0, 0, 0, -1, 0, 0.1) & \text{if } x > 0.5. \end{cases} \quad (66)$$

The experiment takes a ratio of specific heats $\gamma = 2.0$ and is observed at $t = 0.1$. Advancing the numerical solution produces a fast rarefaction, a slow compound wave, a contact discontinuity, and a slowly moving shock with shock speed $S \approx -0.3$. As seen in Figure 11, erroneous oscillations pervade the solution for the Roe and Osher Riemann solvers computed with PPM and the MC slope limiter on a grid size $N = 128$. The error is reduced when computing the slope limiters with an upwind bias. See Figures 11b, 11d, and 12.

By changing the strength of the tangential magnetic field component B_y, the speed of the right-going shock is changed. It is evident from Figure 13 that the size of the oscillations are a function of the shock speed. As the tangential magnetic field strength increases from zero to one and the shock speed decreases, the oscillations increase in amplitude and wavelength.

In Figure 14a, the WENO-type slope limiter's ability to capture MHD physics is demonstrated. Its performance in slowly moving shock regions is comparable to the slope limiters of minmod, MC, and van Leer as illustrated in Figure 14b.

6. Discussion

6.1. Study in phase space

An efficient means of studying the numerics ability to capture the true physics is through a study in phase space. In this section, the numerical solution of the isothermal Euler equations is compared to the exact shock curve
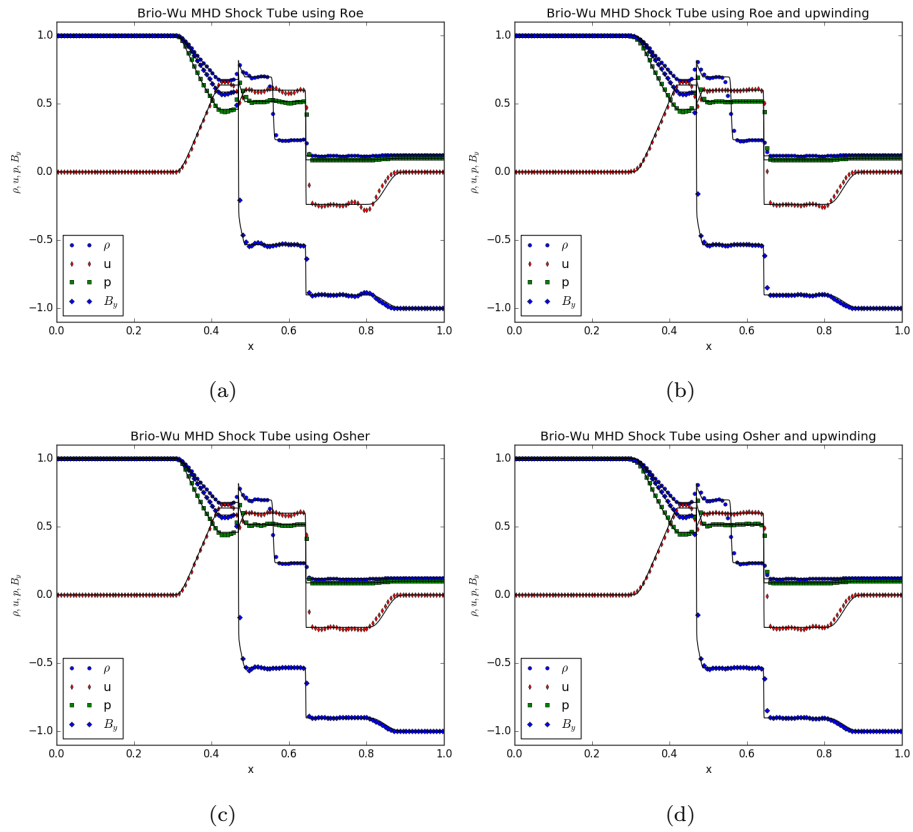
Figure 11: The Brio-Wu MHD shock tube problem at $t = 0.1$. The solutions for (a) Roe, (b) Roe with upwinding, (c) Osher, and (d) Osher with upwinding are computed on a grid size $N = 128$, and compared to WENO-Z with RK4 computed on a grid size of $N = 2048$.
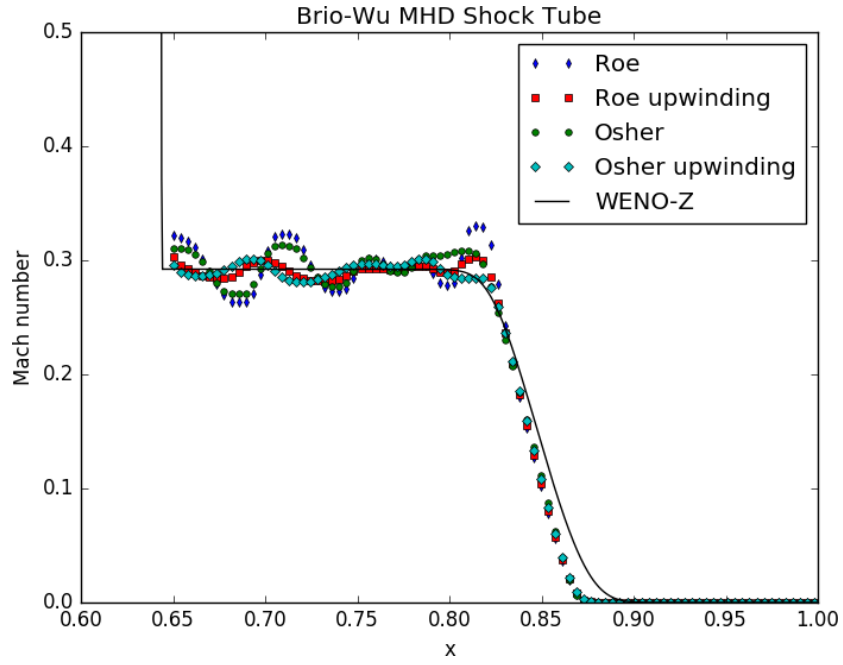
Figure 12: The Brio-Wu shock tube problem. A zoom in on the oscillations in Mach number. The experiment used a grid size of $N = 256$.

Figure 13: Mach number for the Brio-Wu MHD shock tube problem with varying B_y. The solution for (a) Osher, (b) Osher with upwinding are compute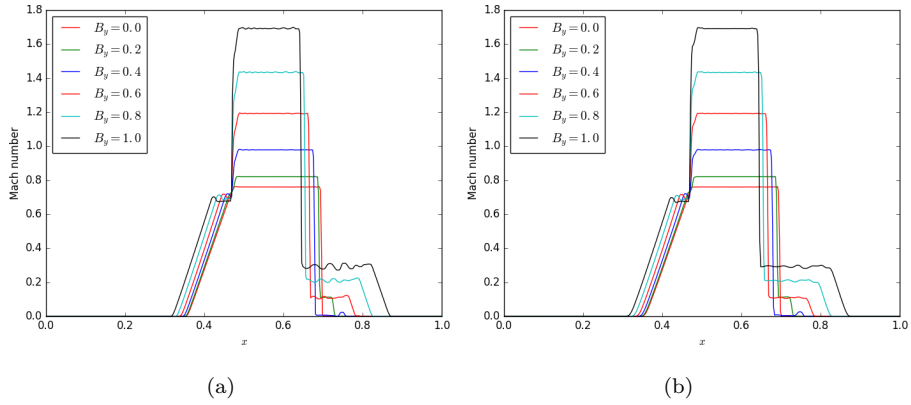d with PPM and MC slope limiter on a grid size of $N = 400$. As the transverse magnetic field strength is increased, the shock speed decreases and the oscillations become more severe.
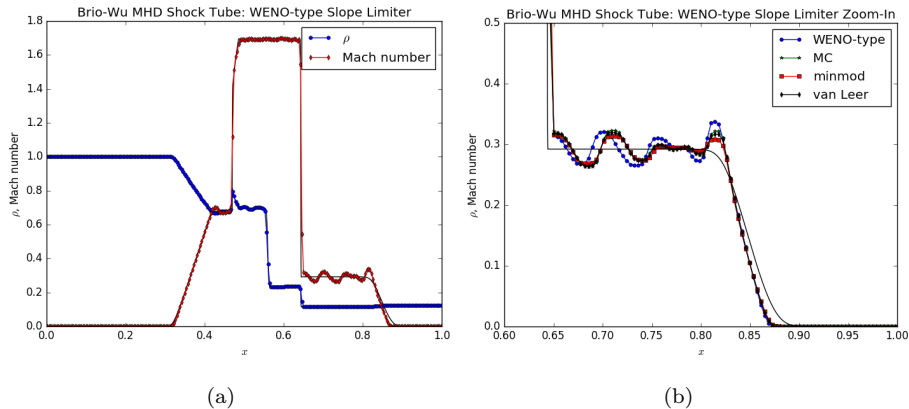
Figure 14: (a) The performance of the WENO-type slope limiter is presented in the Brio-Wu shock tube problem with PPM and Roe on a grid size of $N = 256$. (b) A zoom-in on the oscillations in Mach number for the WENO-type, MC, minmod, and van Leer slope limiters.

determined by the Hugoniot locus. The Hugoniot locus is constructed by considering the set of equilibrium states that can be connected to an adjacent state by a discontinuity satisfying the Rankine-Hugoniot jump condition.

The Rankine-Hugoniot jump condition states the change in flux is proportional to the change in state with the constant of proportion being the shock speed. Fixing $u_L \in \mathbb{R}^N$ and parameterizing the solution $u_{R;k}(c; u_L)$, such that $u_{R;k}(0; u_L) = u_L$, results in a set of N equations with $N + 1$ unknowns: u_R and S. In the case of a linear flux function, the kth wave family has a jump $u_R - u_L$ that is a scalar multiple of the kth right eigenvector, and the shock speed is the kth characteristic speed.

$$u_{R;k}(c; u_L) = u_L + c r_k \tag{67}$$

$$s_k(c; u_L) = \lambda_k \tag{68}$$

These solution curves are lines that connect the left and right states by a 1-shock.

A solution to nonlinear systems is pursued in the same fashion. The Rankine-Hugoniot jump condition,

$$f(u_{R;k}(c; u_L)) - f(u_L) = s_k(u_{R;k}(c; u_L) - u_L), \tag{69}$$

35

is differentiated with respect to constant the c, and then c is set equal to zero:

$$f'(u_{R;k}(0; u_L))u'_{R;k}(0; u_L) - 0 = s_k(u_{R;k}(0; u_L) - 0) \tag{70}$$

$$\implies f'(u_L)u'_{R;k}(0; u_L) = s_k u'_{R;k}(0; u_L). \tag{71}$$

Eq.(71) shows $u'_{R;k}(0; u_L)$ is the kth eigenvector of the Jacobian matrix $f'(u_L)$, and the shock speed is the kth eigenvalue. This means the solution curve $u_{R;k}(c; u_L)$ is tangent to $r_k(u_L)$ at the left state. It can be shown the solution curves exist in a neighborhood around u_L and the functions $u_{R;k}$ and s_k are smooth if the flux function is smooth [43, 44]. If a solution $u_{R;k}(c; u_L)$ lies on the kth Hugoniot curve through u_L, a k-shock is present.

As described in Section 2.1.2, the full Euler equations can be reduced to the isothermal Euler equations by setting $\gamma \approx 1$. This allows for the study of the internal dynamics of the slowly moving shock in the density-momentum phase space. Let momentum be denoted as $m = \rho u$, and apply the Rankine-Hugoniot jump condition to the isothermal Euler equations to get two solution curves:

$$m_R - m_L = s(\rho_R - \rho_L) \tag{72}$$

$$\left(\frac{m_R^2}{\rho_R} + a^2 \rho_R\right) - \left(\frac{m_L^2}{\rho_L} + a^2 \rho_L\right) = s(m_R - m_L) \tag{73}$$

$$\implies \begin{cases} m_R = \frac{\rho_R m_L}{\rho_L} \pm a\sqrt{\frac{\rho_R}{\rho_L}}(\rho_R - \rho_L) \\ s = \frac{m_L}{\rho_L} \pm a\sqrt{\frac{\rho_R}{\rho_L}}. \end{cases} \tag{74}$$

The Hugoniot locus is determined by evaluating the first equation at a set of points ρ_R between the known left and right density values.

In Figure 15, phase plots for the Roe, Osher, and HLLC Riemann solvers with and without upwinding are presented. One interesting feature is the cluster of points near the right state associated with the upwind oscillations. Unlike the numerical orbit near the downwind state u_L, the numerical orbit at the upwind state u_R deviates significantly from the Hugoniot curve for all numerical flux functions. This is a result of small cross characteristic waves influencing the solution in slowly moving shock regions where the shock characteristic is

36

necessarily small. Note that once the upwind-biased slope limiter is implemented the disturbance at the upwind state reduces in size.

In Figure 16, the phase plots for the MC, minmond, van Leer, and WENO-type slope limiters are presented. The numerical orbits for the three standard slope limiters are very similar to each other and the exact shock curve, while the WENO-type slope limiter deviates significantly from the common structure. Based on the numerical tests where there is a shift in the oscillations computed by the new slope limiter, (see Figure 8 and Figure 14) this is not surprising.

6.2. Roberts' argument for a single zone shock layer

Consider the discrete profile of a shock. In order to not produce noise in the solution, all but the shock wave family should vanish in the upwind direction within the discrete shock profile. If more than a shock wave connects the left and right state, then the internal zone of the shock will not move tangent to the shock curve $H(U_L; U_R)$. Since approximate Riemann solvers generate a full wave solution, shock regions are polluted by cross characteristic information.

Roberts [5] recognized the equation of the shock curve passing through U_R in state space must satisfy $H(U; U_R) = 0$. Using the Godunov flux function

$$\hat{F} = \frac{1}{2}(F_R + F_L) - \frac{1}{2}(\Delta F^+ - \Delta F^-),) \tag{75}$$

where $\Delta F^\pm$ is the exact solution to the Riemann problem, he calculated the difference between the post-shock region and the shock front.

$$\delta U_j^n = U_j^{n+1} - U_j^n = \frac{\Delta t}{\Delta x}\left[\hat{F}_{j+\frac{1}{2}}^n - \hat{F}_{j-\frac{1}{2}}^n\right] \tag{76}$$

If a point U_j^n in the shock front lies on the shock curve, then it is required that $H(U_n^j; U_R) = 0$. And consequently, the projection of the gradient of the Hugoniot curve onto the change in state across the shock must be zero.

$$\nabla_U H(U_j^n; U_R) \cdot \delta U_j^n = 0 \tag{77}$$

Eq.(77) can be rewritten with the Godunov flux function as

$$\nabla_U H(U_j^n; U_R) \cdot (\Delta F_{j+\frac{1}{2}}^- + \Delta F_{j-\frac{1}{2}}^+) = 0. \tag{78}$$

37
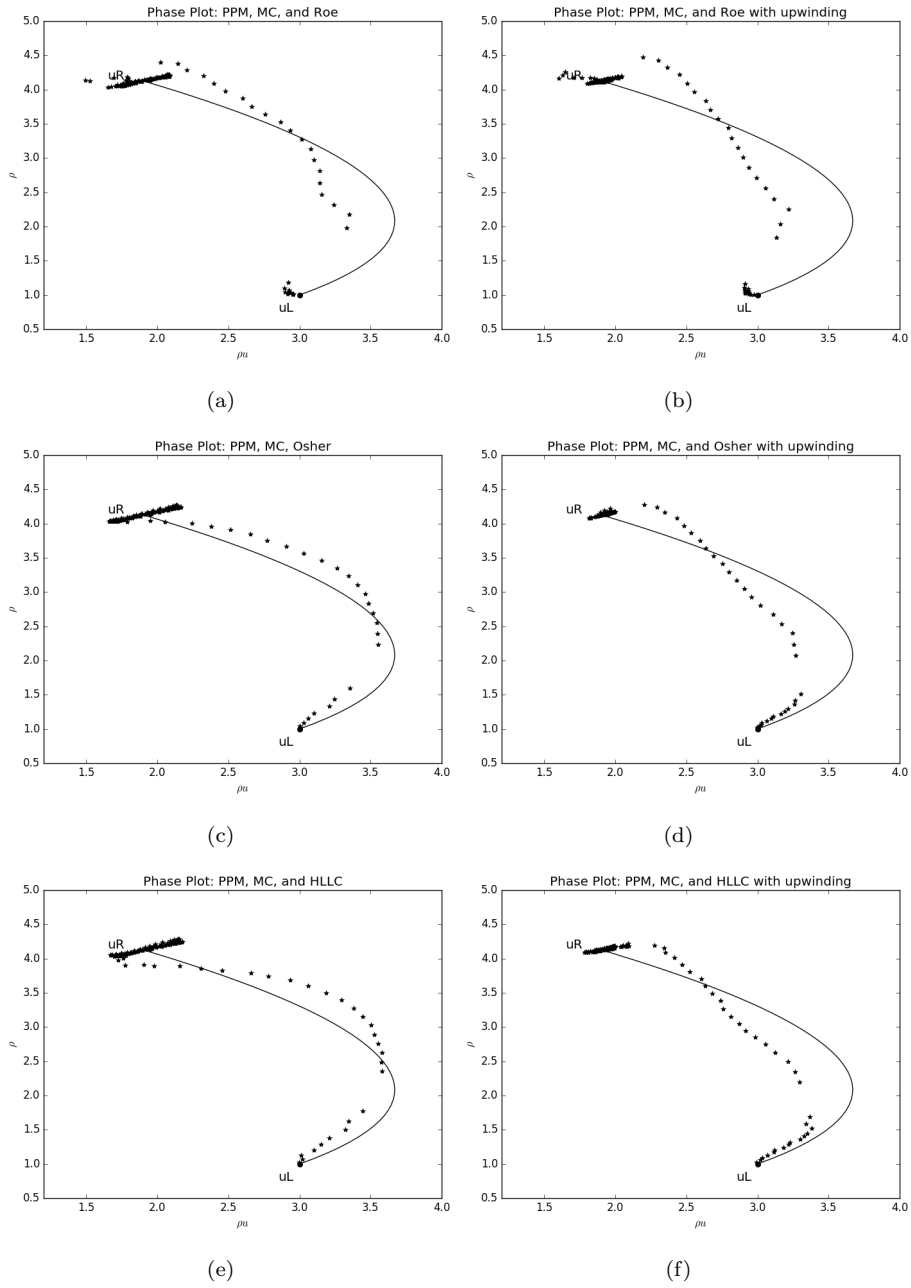
Figure 15: Phase plots of the internal shock structure of the slowly moving shock experiment in hydrodynamics using (a) Roe, (b) Roe and upwinding, (c) Osher, (d) Osher and upwinding, (e) HLLC, and (f) HLLC and upwinding.

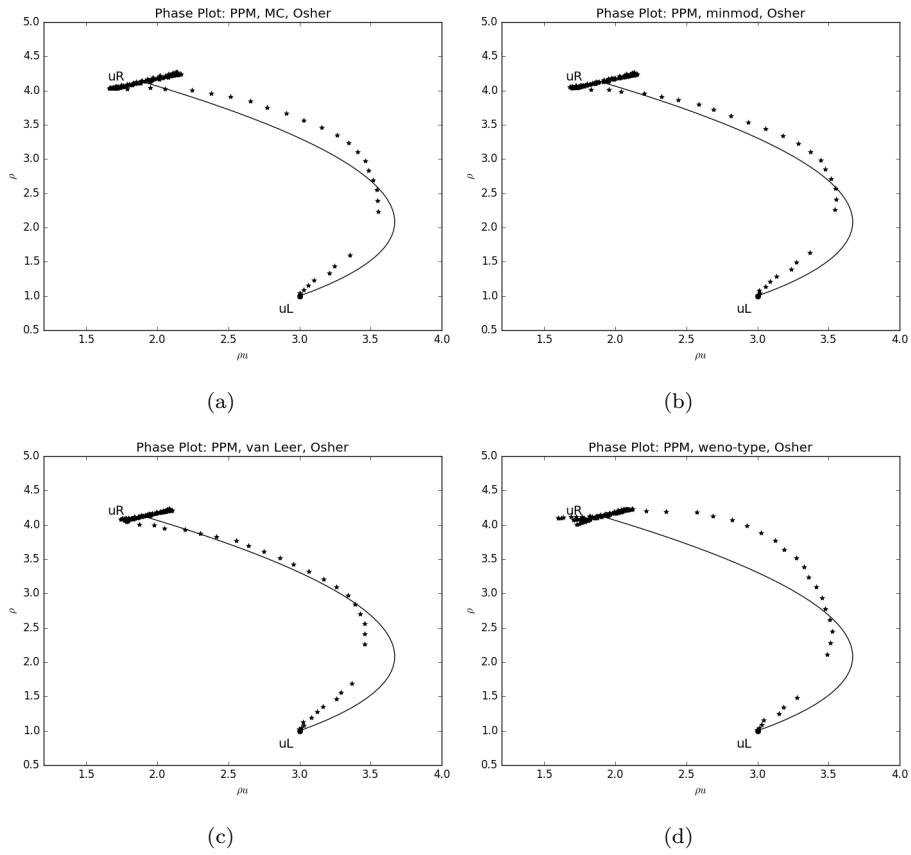Figure 16: Phase plots of the internal shock structure of the slowly moving shock experiment in hydrodynamics. Discrete shock curves are shown for the (a) MC, (b) minmod, (c) van Leer, (d) and WENO-type slope limiters.

The condition in Eq.(78) is dependent on the upwind value U_{j-1}^n, which then effects the internal shock structure. Roberts appropriately concluded no single zone shock layer may satisfy Eq.(77).

Consider a shock with one transition zone U_j^n with left and right states $U_L = U_{j-1}^n$ and $U_R = U_{j+1}^n$. Following Roberts' argument there can be no downwind running waves at $x_{j+\frac{1}{2}}$ or upwind running waves at $x_{j-\frac{1}{2}}$. Eq.(78) reduces to

$$\nabla_U H(U_j^n; U_R) \cdot (F_R - F_L) = 0, \tag{79}$$

where $F_R = F(U_R)$ and $F_L = F(U_L)$. Considering the jump relation $\Delta F = S\Delta U$, the required relationship for no oscillations as stated in Eq.(79) is equivalent to

$$\nabla_U H(U_j^n; U_R) \cdot (U_R - U_L) = 0. \tag{80}$$

The shock curve must remain tangent to the difference between the left and right states of the shock to achieve an accurate solution. Since the Riemann problem returns a full wave solution dependent on a stencil of cells exceeding the shock region, this will not be the case for systems of equations.

6.3. Monotonicity check

The performance of upwinding is dependent on the inclusion of an additional monotonicity check during the construction of the interpolation polynomial. The check, enforced before the final computation of initial Riemann states in Eq.(20), takes the form:

$$u_L = \min(\max(u_i, u_{i-1}), \max(\min(u_i, u_{i-1}), u_L)) \tag{81}$$

$$u_R = \min(\max(u_i, u_{i+1}), \max(\min(u_i, u_{i+1}), u_R)) \tag{82}$$

This condition ensures the left and right Riemann states do not create a new extremum. As depicted in Figure 17, not including this monotonicity check diminishes the upwind-biased slope limiter's ability to reduce the oscillations produced by slowly moving shocks.

The exact role of the monotonicity check needs further investigation. In the 2-dimensional Sedov explosion including the check exaggerates an instability
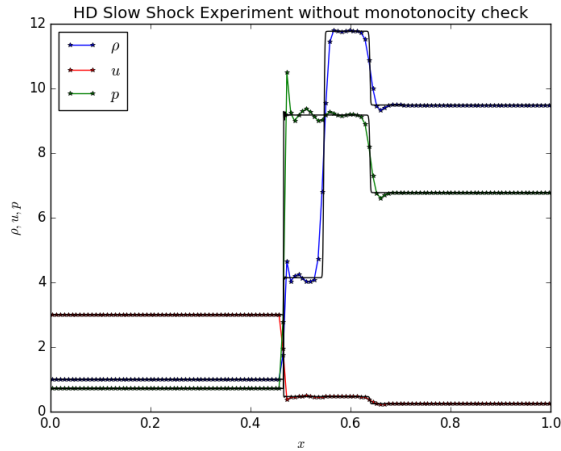
Figure 17: The hydrodynamics slow shock experiment computed with upwinding and without a necessary monotonicity check. The solution is computed with PPM, Roe, and MC slope limiter on a grid size of $N = 128$. Without the additional check a spike forms at the shock front.

that results from solving a spherical problem in cartesian coordinates known as the carbunkle instability. In Figure 18a the Sedov explosion is computed without the monotonicity check, and in Figure 18b it is computed with the monotonicity check. In the latter image symmetric features appear along the x-axis and y-axis due to lack of numerical diffusion along the axes. It has been shown that adding numerical diffusion to experiments that exhibit the carbunkle instability can remove the problem [45].

7. Conclusion

The Rankine-Hugoniot jump condition determines the set of equilibrium points that may exist connecting two states provided a flux function and shock speed. In the case of a scalar equation, two adjacent states are connected exactly by a single wave. In the case of a system of equations, the shock speed changes nonlinearly within the shock zone. Fast shocks move across multiple grid cells in a single time step, so the error produced by discretizing a shock is not prevalent. In contrast, shocks that take multiple time steps to cross a grid cell produce
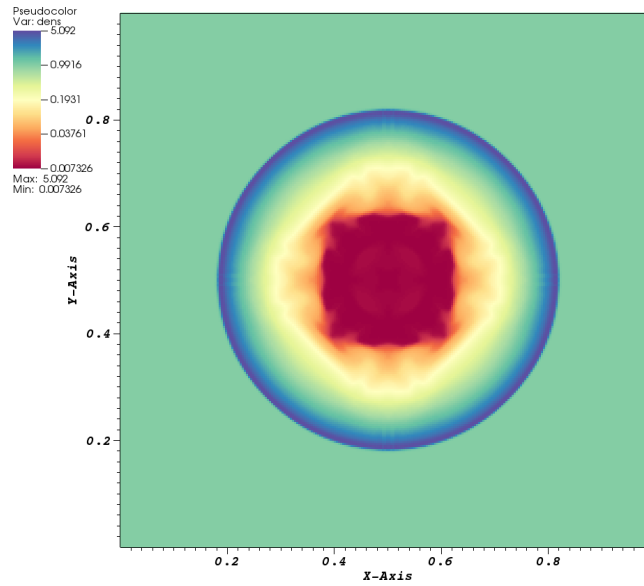
(a)
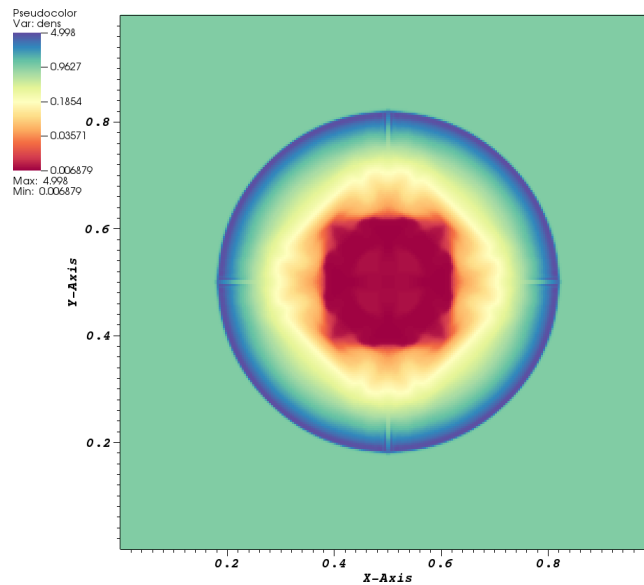
(b)

Figure 18: The Sedov explosion experiment at time $t = 0.1$ on a logarithmic scale (a) without the monotonicity check and (b) with the monotonicity check. The solution is computed with PPM, Roe Riemann solvers, MC slope limiter, and a grid size of $N_x = 256$ and $N_y = 256$.

large unphysical oscillations. As demonstrated in this report, current numerical methods do not intelligently capture the nonlinear internal shock structure.

The numerics studied here provide an improvement to the problem with little additional computational cost. The hybridized upwind-biased slope limiter for PPM [37] is applied to drastically reduce the oscillations produced near slowly moving shocks. It is demonstrated that the universal Osher Riemann solvers [31] perform as well as the Riemann solvers of Roe in smooth flows and moderately better in regions of slow shocks. A WENO-type slope limiter was developed based on a high-order approximation of the slope used in the construction of PCM [19]. Due to computational complexity, the new slope limiter is not deemed the most appropriate solution to the problem.

8. Appendix

8.1. Construction of discrete conservative form

Define a control volume in the space-time domain as $[x_{j-\frac{1}{2}}, x_{j+\frac{1}{2}}] \times [t^n, t^{n+1}]$ and integrate Eq. (3) over a control volume.

$$0 = \int_{x_{j-\frac{1}{2}}}^{x_{j+\frac{1}{2}}} \int_{t^n}^{t^{n+1}} u_t(x,t)dtdx + \int_{x_{j-\frac{1}{2}}}^{x_{j+\frac{1}{2}}} \int_{t^n}^{t^{n+1}} (f(u(x,t)))_x dtdx \tag{83}$$

$$0 = \int_{x_{j-\frac{1}{2}}}^{x_{j+\frac{1}{2}}} u(x,t^{n+1})dx - \int_{x_{j-\frac{1}{2}}}^{x_{j+\frac{1}{2}}} u(x,t^n)dx \tag{84}$$

$$+ \int_{t^n}^{t^{n+1}} (f(u(x_{j+\frac{1}{2}},t)))_x dt - \int_{t^n}^{t^{n+1}} (f(u(x_{j-\frac{1}{2}},t)))_x dt \tag{85}$$

Define a cell-average as

$$\bar{u}_j^n = \int_{x_{j-\frac{1}{2}}}^{x_{j+\frac{1}{2}}} u(x,t^n)dx. \tag{86}$$

and the average flux of u across the right cell-interface for $t^n \leq t^{n+1}$ as

$$F_{j+\frac{1}{2}}^n = \frac{1}{\Delta t} \int_{t^n}^{t^{n+1}} f(u(x_{j+\frac{1}{2}},t))dt. \tag{87}$$

Substituting these into Eq. (85) discovers the discrete conservation law.

$$\bar{u}_j^{n+1} = \bar{u}_j^n - \frac{\Delta t}{\Delta x}\left[F_{j+\frac{1}{2}}^n - F_{j-\frac{1}{2}}^n \right] \tag{88}$$

8.2. Half-time step computation

Compute the half-time step advancement of an mth reconstructed component $v_{i:m}$ on I_i at edges $x = x_{i+\frac{1}{2}}$

$$v_{R,j:m}^{n+\frac{1}{2}} = \frac{1}{\Delta t} \int_{t^n}^{t^{n+1}} p_j(x_{j+\frac{1}{2}})dt \tag{89}$$

$$= \sum_k \frac{1}{\Delta t} \int_{t^n}^{t^{n+1}} r_{j:m}^{(k)} w_j^{(k)}(x_{j+\frac{1}{2}},t)dt \tag{90}$$

$$= \sum_k \frac{1}{\Delta t} \int_{t^n}^{t^{n+1}} r_{j:m}^{(k)} l_j^{(k)} \cdot p_j(x_{j+\frac{1}{2}} - \lambda_j^{(k)}(t-t^n))dt \tag{91}$$

$$= \sum_{k;\lambda_j^{(k)}>0} \frac{1}{\lambda_j^{(k)}\Delta t} \int_{x_{j+\frac{1}{2}}-\lambda_j^{(k)}\Delta t}^{x_{j+\frac{1}{2}}} r_{j:m}^{(k)} l_j^{(k)} \cdot p_j(x)dx \tag{92}$$

44

Consider the integrand of the last line.

$$r_{j:m}^{(k)} l_j^{(k)} \cdot p_j(x) = r_{j:m}^{(k)} l_j^{(k)} \cdot (p_{j:1}, p_{j:2}, p_{j:3})^T \tag{93}$$

$$= r_{j:m}^{(k)} \sum_{s=1}^{3} l_{j:s}^{(k)} (\bar{v}_{j:s}^n + (x - x_j) \frac{\Delta v_{j:s}^n}{\Delta x}) \tag{94}$$

$$= r_{j:m}^{(k)} \sum_{s=1}^{3} l_{j:s}^{(k)} \bar{v}_{j:s}^n + \frac{(x - x_j)}{\Delta x} r_{j:m}^{(k)} \sum_{s=1}^{3} l_{j:s}^{(k)} \Delta v_{j:s}^n \tag{95}$$

Integrate the first term of the last line:

$$\int \left(r_{j:m}^{(k)} \sum_{s=1}^{3} l_{j:s}^{(k)} \bar{v}_{j:s}^n \right) \partial x = \begin{cases} \sum_{k; \lambda^{(k)} > 0} r_{j:m}^{(k)} l_j^{(k)} \cdot \bar{v}_j^n & \text{for Roe,} \\ \sum_{k=1}^{3} r_{j:m}^{(k)} l_j^{(k)} \cdot \bar{v}_j^n & \text{for HLL.} \end{cases} \tag{96}$$

Then, integrate the second term:

$$\int \left(\frac{(x - x_j)}{\Delta x} r_{j:m}^{(k)} \sum_{s=1}^{3} l_{j:s}^{(k)} \Delta v_{j:s}^n \right) = \frac{1}{2} \sum_{k; \lambda_j^{(k)} > 0} \left(1 - \frac{\lambda_j^{(k)} \Delta t}{\Delta x} \right) r_{j:m}^{(k)} \Delta w_j^{(k)}. \tag{97}$$

And define $\Delta w_j^{(k)}$:

$$\Delta w_j^{(k)} = \sum_{s=3}^{3} l_{j:s}^{(k)} \Delta v_{j:s}^n = l^{(k)} \cdot \Delta v_j^n \tag{98}$$

$$= \text{TVD} \left[l_j^{(k)} \cdot (v_{j+1}^n - v_j^n), l_j^{(k)} \cdot (v_j^n - v_{j-1}^n) \right] \quad \text{characteristic slope limiting,} \tag{99}$$

$$= l_j^{(k)} \cdot \text{TVD} \left[v_{j+1}^n - v_j^n, v_j^n - v_{j-1}^n \right] \quad \text{primitive slope limiting.} \tag{100}$$

8.3. Construction of universal Osher Riemann solvers

For completeness and motivation the standard Osher-Solomon Riemann solvers [28, 29] formulation is constructed. Assume flux splitting

$$F(U) = F^+(U) + F^-(U), \tag{101}$$

45

where the positive flux function has a Jacobian matrix with positive eigenvalues and the negative flux function has a Jacobian matrix with negative eigenvalues.

$$A^+(U) = \frac{\delta F^+(U)}{\delta U}, \text{ and } A^-(U) = \frac{\delta F^-(U)}{\delta Q} \tag{102}$$

Then the Osher-Solomon flux is $F_{j+\frac{1}{2}}(U_L, U_R) = F^+(U_L) + F^-(U_R)$. This relation is determined by taking a path independent integral connecting the left and right states in phase space.

$$\int_{U_L}^{U_R} A^-(U)dU = F^-(U_R) - F^-(U_L) \tag{103}$$

$$\int_{U_L}^{U_R} A^+(U)dU = F^+(U_R) - F^+(U_L) \tag{104}$$

Using these relations it is easily shown that

$$F_{i+\frac{1}{2}} = F(U_L) + \int_{U_L}^{U_L} A^-(U)dU \tag{105}$$

$$= F(U_R) - \int_{U_L}^{U_R} A^+(U)dU \tag{106}$$

$$= \frac{1}{2}\left(F(U_L) + F(U_R)\right) - \frac{1}{2}\int_{U_L}^{U_R} |A(U)|dU \tag{107}$$

The path of integration is chosen to be a union of disjoint line segments connecting each characteristic field. Intermediate states are determine assuming a simple wave connects each field. Genuinely nonlinear fields require splitting the path in two connected by a sonic point. The intersection points and sonic points must be explicitly defined for each hyperbolic system. The integration partial paths may have many different cases based on the wave structure. For example, the Euler equations have 16 cases.

The universal Osher-type method [31] is independent of system structure and is complete, it considers all wave information when solving the Riemann problem. The messy integration in the original method is performed on a line segment in phase space $\Psi(s)$,

$$\Psi(s) = U_L + s(U_R - U_L), \quad 0 \le s \le 1 \tag{108}$$

46

evaluated at points determined by a Gauss-Legendre quadrature rule.

$$F_{i+\frac{1}{2}} = \frac{1}{2}\left(F(U_L) + F(U_R)\right) - \frac{1}{2}\int_{U_L}^{U_R}|A(U)|dU \tag{109}$$

$$= \frac{1}{2}\left(F(U_L) + F(U_R)\right) - \frac{1}{2}\int_{U_L}^{U_R}|A(\Psi(s))|\frac{\partial\Psi}{\partial s}ds \tag{110}$$

$$= \frac{1}{2}\left(F(U_L) + F(U_R)\right) - \frac{1}{2}\left(\int_{U_L}^{U_R}|A(\Psi(s))|ds\right)(U_R - U_L) \tag{111}$$

$$= \frac{1}{2}\left(F(U_L) + F(U_R)\right) - \frac{1}{2}\left|\int_{U_L}^{U_R}A(\Psi(s))ds\right|(U_R - U_L) \tag{112}$$

The integrand and absolute value lead to complicated expressions. The generalized Osher flux simplifies the calculation by considering a Gaussian rule with g points s_j and associated weight w_j.

$$F_{i+\frac{1}{2}}\left(F(U_L) + F(U_R)\right) - \frac{1}{2}\left(\sum_{i=1}^{g}w_j|A((\Psi(s_j))|\right)(U_R - U_L) \tag{113}$$

The intermediate states on path $\Psi(s_j)$ lie in the domain of possible solutions, a convex region. The system is hyperbolic for all possible solutions within this domain, so the matrix $A(\Psi(s_j))$ is hyperbolic for all intermediate points.

References

[1] P. Woodward, P. Colella, The numerical simulation of two-dimensional fluid flow with strong shocks, Journal of computational physics 54 (1) (1984) 115–173.

[2] S. Karni, S. Čanić, Computations of slowly moving shocks, Journal of Computational Physics 136 (1) (1997) 132–139.

[3] M. Arora, P. L. Roe, On postshock oscillations due to shock capturing schemes in unsteady flows, Journal of Computational Physics 130 (1) (1997) 25–40.

[4] S. Billett, E. Toro, Restoring monotonicity of slowly-moving shocks computed with godunov-type schemes, NASA STI/Recon Technical Report N 93 (1992) 24075.

[5] T. W. Roberts, The behavior of flux difference splitting schemes near slowly moving shock waves, Journal of Computational Physics 90 (1) (1990) 141–160.

[6] S. Jin, J.-G. Liu, The effects of numerical viscosities: I. slowly moving shocks, Journal of Computational Physics 126 (2) (1996) 373–389.

[7] E. Johnsen, S. Lele, Numerical errors generated in simulations of slowly moving shocks, Center for Turbulence Research, Annual Research Briefs (2008) 1–12.

[8] M. Siklosi, G. Kreiss, Elimination of first order errors in time dependent shock calculations, SIAM journal on numerical analysis 41 (6) (2003) 2131–2148.

[9] Y. Stiriba, R. Donat, A numerical study of postshock oscillations in slowly moving shock waves, Computers & Mathematics with Applications 46 (5-6) (2003) 719–739.

[10] G. Tóth, X. Meng, T. I. Gombosi, A. J. Ridley, Reducing numerical diffusion in magnetospheric simulations, Journal of Geophysical Research: Space Physics 116 (A7).

[11] D. Ryu, T. Jones, Numerical magnetohydrodynamics in astrophysics: algorithm and tests for one-dimensional flow, arXiv preprint astro-ph/9404074.

[12] R. J. LeVeque, R. J. Leveque, Numerical methods for conservation laws, Vol. 132, Springer, 1992.

[13] R. J. LeVeque, Finite volume methods for hyperbolic problems, Vol. 31, Cambridge university press, 2002.

[14] R. M. Mattheij, S. W. Rienstra, J. H. ten Thije Boonkkamp, Partial differential equations: modeling, analysis, computation, Siam, 2005.

[15] A. Bressan, Hyperbolic conservation laws: an illustrated tutorial, in: Modelling and Optimisation of Flows on Networks, Springer, 2013, pp. 157–245.

[16] S. K. Godunov, A difference method for numerical calculation of discontinuous solutions of the equations of hydrodynamics, Matematicheskii Sbornik 89 (3) (1959) 271–306.

[17] B. Van Leer, P. Woodward, The muscl code for compressible flow: Philosophy and results, in: Proc. TICOM Conf., Austin, Texas, 1979.

[18] P. Colella, P. R. Woodward, The piecewise parabolic method (ppm) for gas-dynamical simulations, Journal of computational physics 54 (1) (1984) 174–201.

[19] D. Lee, H. Faller, A. Reyes, The piecewise cubic method (pcm) for computational fluid dynamics, Journal of Computational Physics 341 (2017) 230–257.

[20] X.-D. Liu, S. Osher, T. Chan, Weighted essentially non-oscillatory schemes, Journal of computational physics 115 (1) (1994) 200–212.

[21] G.-S. Jiang, C.-W. Shu, Efficient implementation of weighted eno schemes, Journal of computational physics 126 (1) (1996) 202–228.

[22] J. Shi, C. Hu, C.-W. Shu, A technique of treating negative weights in weno schemes, Journal of Computational Physics 175 (1) (2002) 108–127.

[23] M. Castro, B. Costa, W. S. Don, High order weighted essentially non-oscillatory weno-z schemes for hyperbolic conservation laws, Journal of Computational Physics 230 (5) (2011) 1766–1792.

[24] A. Reyes, D. Lee, C. Graziani, P. Tzeferacos, A new class of high-order methods for fluid dynamics simulations using gaussian process modeling: I. one-dimensional case, arXiv preprint arXiv:1611.08084.

[25] B. Fryxell, K. Olson, P. Ricker, F. Timmes, M. Zingale, D. Lamb, P. MacNeice, R. Rosner, J. Truran, H. Tufo, Flash: An adaptive mesh hydrodynamics code for modeling astrophysical thermonuclear flashes, The Astrophysical Journal Supplement Series 131 (1) (2000) 273.

[26] B. Van Leer, Towards the ultimate conservative difference scheme. v. a second-order sequel to godunov's method, Journal of computational Physics 32 (1) (1979) 101–136.

[27] P. L. Roe, Approximate riemann solvers, parameter vectors, and difference schemes, Journal of computational physics 43 (2) (1981) 357–372.

[28] S. Osher, F. Solomon, Upwind difference schemes for hyperbolic conservation laws, Mathematics of Computation 38 (339-374).

[29] S. Osher, Riemann solvers, the entropy condition, and difference approximations, SIAM Journal on Numerical Analysis 21(2) (217-235).

[30] M. J. Castro, J. M. Gallardo, A. Marquina, Approximate osher–solomon schemes for hyperbolic systems, Applied Mathematics and Computation 272 (2016) 347–368.

[31] M. Dumbser, E. F. Toro, On universal osher-type schemes for general nonlinear hyperbolic conservation laws, Communications in Computational Physics 10 (3) (2011) 635–671.

[32] M. Siklosi, B. Batzorig, G. Kreiss, An investigation of the internal structure of shock profiles for shock capturing schemes, Journal of computational and applied mathematics 201 (1) (2007) 8–29.

[33] E. Johnsen, S. K. Lele, J. Larsson, Analysis and correction of errors generated by slowly moving shocks, in: 49th AIAA Aerospace Sciences Meeting, Vol. 657, 2011.

[34] E. Johnsen, Analysis of numerical errors generated by slowly moving shock waves, AIAA journal 51 (5) (2013) 1269–1274.

[35] C.-W. Shu, S. Osher, Efficient implementation of essentially non-oscillatory shock-capturing schemes, Journal of Computational Physics 77 (2) (1988) 439–471.

[36] A. Marquina, Local piecewise hyperbolic reconstruction of numerical fluxes for nonlinear scalar conservation laws, SIAM Journal on Scientific Computing 15 (4) (1994) 892–915.

[37] D. Lee, An upwind slope limiter for ppm that preserves monotonicity in magnetohydrodynamics, in: 5th International Conference of Numerical Modeling of Space Plasma Flows (ASTRONUM 2010), Vol. 444, 2011, p. 236.

[38] D. Lee, H. Faller, A. Reyes, The piecewise cubic method (pcm) for computational fluid dynamics, arXiv preprint arXiv:1610.05848.

[39] C.-W. Shu, High-order finite difference and finite volume weno schemes and discontinuous galerkin methods for cfd, International Journal of Computational Fluid Dynamics 17 (2) (2003) 107–118.

[40] G. A. Sod, A survey of several finite difference methods for systems of nonlinear hyperbolic conservation laws, Journal of computational physics 27 (1) (1978) 1–31.

[41] C.-W. Shu, S. Osher, Efficient implementation of essentially non-oscillatory shock-capturing schemes, ii, Journal of Computational Physics 83 (1) (1989) 32–78.

[42] M. Brio, C. C. Wu, An upwind differencing scheme for the equations of ideal magnetohydrodynamics, Journal of computational physics 75 (2) (1988) 400–422.

[43] J. Smoller, Shock waves and reaction—diffusion equations, Vol. 258, Springer Science & Business Media, 2012.

[44] P. D. Lax, Hyperbolic systems of conservation laws ii, Communications on pure and applied mathematics 10 (4) (1957) 537–566.

[45] I. Y. Tagirova, A. Rodionov, Application of artificial viscosity for suppressing the carbuncle phenomenon in godunov-type schemes, Mathematical Models and Computer Simulations 8 (3) (2016) 249–262.